



The influence of ammonia emissions on the size-resolved global atmospheric aerosol composition and acidity

Xurong Wang¹, Alexandra P. Tsimpidi¹, Zhenqi Luo², Benedikt Steil³, Andrea Pozzer³, Jos Lelieveld^{3,4}, and Vlassis A. Karydis¹

¹ Institute of Climate and Energy Systems: Troposphere (ICE-3), Forschungszentrum Jülich GmbH, Jülich, Germany

² School of Integrative Plant Science, Soil and Crop Sciences Section, Cornell University, Ithaca, NY 14853, United States of America

³ Max Planck Institute for Chemistry, Atmospheric Chemistry Dept., Mainz, Germany.

⁴ The Cyprus Institute, Climate and Atmosphere Research Center Nicosia, Nicosia, Cyprus.

Correspondence to:

Vlassis A. Karydis (v.karydis@fz-juelich.de) and Alexandra P. Tsimpidi (a.tsimpidi@fz-juelich.de)

Abstract. Ammonia (NH₃) is an abundant alkaline gas in the atmosphere and a key precursor in the formation of particulate matter. While emissions of other aerosol precursors such as SO₂ and NO_x have decreased significantly, global NH₃ emissions are stable or increasing, and this trend is projected to continue. This study investigates the impact of NH₃ emission changes on size-resolved aerosol composition and acidity using the atmospheric chemistry-climate model EMAC. Three NH₃ emission schemes are analyzed: two bottom-up inventories and one derived using an updated top-down method. The results reveal that sulphate-nitrate-ammonium aerosols in two fine mode size ranges (0-1 μm and 1-2.5 μm) show the greatest sensitivity to NH₃ emission changes. Regional responses vary depending on the local chemical environment of secondary inorganic aerosols. In 'NH₃-rich' regions (e.g. East Asia and Europe), the abundance of NH₃ partially offsets the effects of reduced NH₃ emissions when NO_x and SO₂ are available, especially for aerosols in the 1-2.5 μm range. This highlights the importance of coordinated control strategies for NH₃, NO_x and SO₂ emissions. Further, we find that NH₃ has a buffering effect in densely populated areas, maintaining aerosol acidity at moderate levels and mitigating drastic pH shifts. The study emphasizes that pH changes are closely related to NH₃ emission variations, with the highest sensitivity observed in the fine mode size ranges. These results highlight the critical role of NH₃ in shaping aerosol acidity and argue for size-specific approaches to managing particulate matter.

1. Introduction

As an abundant alkaline gas in the atmosphere, ammonia (NH₃) acts as a precursor in the formation of particulate matter by neutralizing atmospheric acids (e.g., H₂SO₄, HNO₃) to form sulfate-nitrate-ammonium (SNA) aerosols (Li et al., 2018; Chen et al., 2016; Wang et al., 2013), which are the main secondary inorganic components of PM_{2.5} (particulate matter with a diameter of 2.5 μm or less). By condensing onto freshly nucleated particles, NH₃ enhances the growth rate of new particles as well as their hydrophilicity (Wang et al., 2020; Li et al., 2018). This can degrade air quality and change the solar radiative balance by interaction with radiation and clouds (Che et al., 2009; Zhao et al., 2011; Yao et al., 2018). In addition, the conjugate base-acid pair NH₃/NH₄⁺ acts as the major buffer that inhibits changes in aerosol acidity (Chen et al., 2019; Zheng et al., 2020; Karydis et al., 2021).



Anthropogenic emissions are the main source of atmospheric NH_3 , with an average global contribution of 76%,
 40 dominated by agricultural activities, including livestock farming and the fertilization of soils (Schlesinger and Hartley,
 1992; Dentener and Crutzen, 1994; Bouwman et al., 1997; Olivier et al., 1998; Van Aardenne et al., 2001; Bleeker et
 al., 2013). Meanwhile, the importance of non-agricultural sources, such as industrial emissions and fossil fuel
 combustion, has been highlighted by studies focusing on severe haze episodes in East Asia (Chang et al., 2019; Liu et
 al., 2018a; Pan et al., 2016). The construction of high-resolution regional or global datasets has characterized the
 45 spatiotemporal patterns of NH_3 emissions, with the most common datasets consisting of bottom-up inventories and
 top-down modeling inversion methods. Bottom-up emission inventories rely on activity data and emission factors, the
 latter being sensitive to assumptions about fertilizer types, local soil and meteorological properties (Bouwman et al.,
 2002; Sogaard et al., 2002; Xu et al., 2024). Zhang et al. (2018) evaluated discrepancies between bottom-up NH_3
 emission inventories to exceed a factor of two, due to the uncertainties in emission factors, meteorological properties,
 50 and agricultural statistics (Beusen et al., 2008). Crippa et al. (2018) pointed out that the uncertainty in estimated NH_3
 emissions is largest among all pollutants in the Emissions Database for Global Atmospheric Research (EDGAR
 v4.3.2), with a range of variation from 186% to 294% in 2012. In contrast, the ability of satellites to measure NH_3
 abundance combined with numerical simulations allows a better characterization of the spatial distribution and
 seasonality of NH_3 emissions, but the low signal-to-noise ratio over low-emission areas limits the accuracy of retrieval
 55 products (Morán et al., 2016; Xu et al., 2016; Kong et al., 2019). Using a hybrid inverse modeling approach, Chen et
 al. (2021) optimized the NH_3 emission inventory NEI over the United States by combining CMAQ model simulations
 with constraints from the Infrared Atmospheric Sounding Interferometer (IASI) retrieval product. They found a 26%
 low bias of NH_3 emissions in the NEI, and the optimized NH_3 emission inventory improved the model performance
 of $\text{PM}_{2.5}$ mass concentration in the Midwest US, and the normalized mean bias of NH_4^+ and NO_3^- decreased from 27%
 60 to 22%, and 64% to 55%, respectively.

Recently, the emissions of SO_2 and NO_x have decreased due to the implementation of related clean air policies in
 East Asia, North America and Europe (Zheng et al., 2018; Hand et al., 2012; Russell et al., 2012; Aas et al., 2019;
 Gong et al., 2024), while the emissions of NH_3 remained stable or have slightly increased in major agricultural regions
 such as China (Xu et al., 2016), the United States (Yu et al., 2018), and Europe (Fortems-Cheiney et al., 2022). The
 65 increase in NH_3 emissions is associated with increasing fertilizer use and local temperatures (Warner et al., 2017; Xu
 et al., 2016; Skjæth and Geels, 2013; Xu et al., 2019), and such trends are expected to continue on a global scale
 throughout the century (IPCC, 2013). Driven by such emission trend of SO_2 , NO_x , and NH_3 , the main composition of
 SNA has changed in large regions with a shift from an ammonium sulfate to an ammonium nitrate formation regime
 (Lei et al., 2021; Jo et al., 2020; Zhou et al., 2019; Shah et al., 2018; Wang et al., 2013; Hauglustaine et al., 2014). Li
 et al. (2017) evaluated that during the period 1989 to 2013, the increasing trend of sulfate (SO_4^{2-}) and ammonium
 70 (NH_4^+) mass concentration in India and China occurred at a rate $>0.1 \mu\text{g m}^{-3} \text{ yr}^{-1}$, while decreasing trends were found
 in North America and Europe at a rate of about $0.1 \mu\text{g m}^{-3} \text{ yr}^{-1}$. The reduction of SO_2 and NO_x results in excess NH_3
 being released to the atmosphere because less NH_3 is required to neutralize H_2SO_4 and HNO_3 , which in turn hinders
 the formation of NH_4^+ in the aerosol phase and increases the atmospheric NH_3 concentration (Liu et al., 2018b). Warner
 et al. (2017) assessed that the average increase rate of NH_3 mass concentration from 2002 to 2016 in the United States,
 75



Europe, and China was 2.6% yr⁻¹, 1.8% yr⁻¹, and 2.3% yr⁻¹, respectively. Some studies further pointed out that the increase in NH₃ concentration may offset the effectiveness of PM_{2.5} control achieved via SO₂ and NO_x emission reduction by promoting the formation of nitrate (NO₃⁻) (Huang et al., 2021; Cai et al., 2017; Zhang and Geng, 2019; Fu et al., 2017).

80 Several studies concluded that reducing NH₃ emissions would be a cost-effective way to control PM_{2.5} concentrations (Gu et al., 2021; Tsimpidi et al., 2007; Erisman and Schaap, 2004). However, the response of SNA to changes in its precursors is not linear (Pozzer et al., 2017; Wang et al., 2011; Wang et al., 2013; West et al., 1999), because the gas-particle partitioning of NH₃/NH₄⁺ and HNO₃/NO₃⁻ is influenced by several parameters, such as temperature, liquid water content, and aerosol acidity (Xu et al., 2020; Nenes et al., 2020; Guo et al., 2018). Nenes et al. (2020) developed a conceptual framework to describe the sensitivity of particulate matter to NO_x and NH₃ emissions, highlighting the critical influence of aerosol acidity and liquid water content on particulate matter formation. Based on sensitivity tests, Guo et al. (2018) evaluated that the response of NO₃⁻ to NH₃ reduction shows an apparent decrease only when the aerosol pH falls below the value of 3.

On the other hand, reductions in SO₂ and NO_x emissions are expected to reduce aerosol acidity, but recent studies 90 revealed that aerosol acidity does not decrease as expected (Chen et al., 2019; Guo et al., 2017a; Zheng et al., 2022; Karydis et al., 2021). Aerosol acidity affects many processes involving the atmosphere and various aspects of the Earth system (Pye et al., 2020; Tilgner et al., 2021; Karydis et al., 2021) as well as human health (Dockery et al., 1993; Dockery et al., 1996; Thurston et al., 1994; Spengler et al., 1996). Weber et al. (2016) found that the acidity of PM_{2.5} in the southeastern United States remained at a relatively constant level with a pH value of 0 – 2 over the past 15 years, despite a 70% reduction in SO₄²⁻ concentration. A lack of aerosol acidity trend was also reported in China (Zhou et al., 2022). This is mainly caused by the buffering effect of NH₃/NH₄⁺ (Chen et al., 2019; Zheng et al., 2022; Zheng et al., 2020). To investigate this, Song et al. (2019) derived an equation from the partitioning of NH₃, and estimated that a unit increase in pH requires a tenfold increase in NH₃ concentration, which is consistent with the findings of Guo et al. (2017a). The regional variation of aerosol acidity is considerable, and the pH of PM_{2.5} in northern China is in the 100 range of 4 to 5, which is higher than in Europe and the United States (Shi et al., 2019; Shi et al., 2017; Liu et al., 2017; Guo et al., 2015; Guo et al., 2016; Guo et al., 2017b; Karydis et al., 2021). This is caused by multiple driving factors, including aerosol mass concentration and composition, NH₃ mass concentration, aerosol water content, and meteorological factors (Ding et al., 2019; Zhang et al., 2021a). However, the main driver for the difference in aerosol acidity remains controversial. Zheng et al. (2020) pointed out that aerosol water content is the most important factor causing the regional variation of aerosol acidity, while Zhang et al. (2021a) emphasized the equal importance of 105 aerosol mass concentration and chemical composition for the aerosol acidity contrasts between China and the United States.

Almost all recent studies that discuss the response of aerosol composition and acidity to changes in NH₃ emission trends focus on the fine mode (e.g. PM_{2.5}). The size-resolved composition of SNA is not uniform (Karydis et al., 2016; Fang et al., 2017; Karydis et al., 2011; Karydis et al., 2010; Guo et al., 2017b), and NH₄⁺ and SO₄²⁻ are mainly concentrated in the fine mode (Wang et al., 2012; Seinfeld and Pandis, 2016), while NO₃⁻ aerosol can be formed on the surface of super-micron particles via heterogeneous chemistry (Allen et al., 2015). Furthermore, Milousis et al.



(2024) revealed that the acidity of fine-mode aerosol is more sensitive to NH_3 emission than coarse-mode aerosol. Reducing the NH_3 emissions by half, the simulated pH of fine and coarse mode aerosol decreased by up to 3 and 1.5 units, respectively. Aerosol acidity tends to decrease with increasing particle size, with pH varying up to 6 units (Craig et al., 2018; Fang et al., 2017; Bougiatioti et al., 2016). Size-resolved aerosol acidity is associated with different formation pathways (Tilgner et al., 2021; Cheng et al., 2016). Ding et al. (2019) found that the coarse-mode aerosol shifted from neutral to weakly acidic with the increase of NO_3^- and SO_4^{2-} during severe hazy days. Cheng et al. (2016) further pointed out that the dominant oxidant in SO_4^{2-} production by SO_2 oxidation changes with the ambient aerosol acidity. Therefore, it is necessary to comprehensively investigate the response of size-resolved chemical composition and acidity to changes in NH_3 emissions.

In this study, three different NH_3 emission schemes are used as input to the atmospheric chemistry–climate model EMAC (ECHAM5/MESSy Atmospheric Chemistry). The three emission schemes include two bottom-up emission inventories (CAMS and CEDS_GBD), and an updated emission inventory produced following a top-down method (Luo et al., 2022). Satellite retrievals of NH_3 column concentrations and aerosol composition observational datasets from multiple sites around the world are used to evaluate the aerosol simulations derived from the three NH_3 emission schemes. We investigate the response of size-resolved aerosol SNA composition and acidity to changes in NH_3 emissions across three well-characterized, anthropogenically polluted regions in the Northern Hemisphere. These regions, representing a gradient from relatively less to more polluted conditions, include the United States, Europe, and the North China Plain. The examined aerosol sizes range (diameter) from sub-micron ($0 - 1 \mu\text{m}$) to super-micron ($1 - 2.5 \mu\text{m}$, $2.5 - 5 \mu\text{m}$, and $5 - 10 \mu\text{m}$).

2. Modelling description

EMAC (ECHAM5/MESSy) is a global atmospheric chemistry and climate model, which includes a number of submodels describing atmospheric processes and interactions among oceans, land, and anthropogenic influences (Jöckel et al., 2016). These submodels are linked to the base model, the 5th generation European Centre Hamburg general circulation model (Roeckner et al., 2006), via the Modular Earth Submodel System (Jöckel et al., 2005). In this study, the horizontal resolution of the EMAC model is T63L31, which corresponds to a grid resolution of about $1.875^\circ \times 1.875^\circ$ (Jöckel et al., 2010) and 31 vertical layers extending up to 25 km altitude. EMAC is applied for 4 years, from 2009 to 2012 with the first year used as a spin-up. The meteorological reanalysis data ERA5 (Hersbach et al., 2020), with a significantly enhanced horizontal resolution of 31 km and hourly output throughout, is used in EMAC to nudge the simulation.

In EMAC, organic aerosol (OA) formation is simulated by the ORACLE module (Tsimpidi et al., 2014; Tsimpidi et al., 2016), where logarithmically spaced saturation concentration bins are used to describe the organic aerosol components based on their volatility. The aerosol microphysics and gas/aerosol partitioning are calculated by the Global Modal-aerosol eXtension (GMXe) module described by Pringle et al. (2010), which has the same microphysical core as the M7 sub-model (Vignati et al., 2004). The aerosol size distribution is treated by 7 log-normal modes, including 4 hydrophilic and 3 hydrophobic modes, covering nucleation (soluble only), Aitken, accumulation, and coarse modes (both soluble and insoluble). To determine size-resolved aerosol composition and pH, we sum the



contributions of each aerosol component, water content, and H^+ concentration across all GMXe modes corresponding to a given size range. This is achieved by calculating the volume fraction of the lognormal distribution of each mode that falls within the specified size limits. The atmospheric chemistry module MECCA (Module Efficiently Calculating the Chemistry of the Atmosphere), which contains a comprehensive atmospheric reaction is used to calculate the gas concentrations (Sander et al., 2019). The SEDI module is used to compute aerosol particle sedimentation (Kerkweg et al., 2006). Dry deposition and wet deposition of gas and particle species are calculated by the DRYDEP module (Kerkweg et al., 2006) and the SCAV module (Tost et al., 2006), respectively. The CLOUD submodel (Roeckner et al., 2006) is used to calculate cloud properties and microphysics, utilizing the microphysical scheme of Lohmann and Ferrachat (2010) and a physically based treatment of liquid (Karydis et al., 2017) and ice crystal (Bacer et al., 2018) activation processes.

An advanced parameterization scheme is incorporated into the EMAC model to calculate the dust emission flux online (Astitha et al., 2012). The scheme uses the online meteorological fields from the EMAC model, such as temperature, pressure, relative humidity, soil moisture, and surface friction velocity, to calculate the threshold friction velocity which is the initial step of dust production. Above the threshold friction velocity, dust emission is possible. Following Karydis et al. (2016), the emissions of individual crustal species in this study are estimated as constant fractions of the dust emission (Klingmüller et al., 2018). These fractional factors depend on the geological information, which includes different dust emission sources. Karydis et al. (2021) pointed out that the crustal ions (Ca^{2+} , Mg^{2+} , K^+ , and Na^+), especially Ca^{2+} , have significantly contributed to maintaining the particle pH value at the level of 4.5 – 5 in East Asia during the last decade. The importance of crustal ions in determining aerosol acidity and factors such as liquid water content, aerosol mass concentration, and chemical composition, has been highlighted in other studies (Zheng et al., 2020; Zhang et al., 2021a; Ding et al., 2019).

2.1 NH_3 emission scheme

In this study, three NH_3 emission schemes are applied in specific model simulation cases to quantify the impact of changes in NH_3 emissions on aerosol composition and acidity (Table 1), which are divided into Bottom-up and Top-down schemes.

Table 1. Setups for simulation cases.

Simulation Case	NH_3 Emission Scheme	Equilibrium State
Base	CAMS-GLOB-ANT, CAMS-GLOB-AIR, GEIA, biomass burning	Stable
CEDS	Same as Base case, but NH_3 , SO_2 , and NO_x are from CEDS-GBD	Stable
Top-Dep	Luo's method with the lifetime derived from deposition, GEIA-water	Stable
Meta	Same as Base case	Metastable
no NH_3	No NH_3 emission input	Stable

2.1.1 Bottom-up scheme

Bottom-up schemes are applied in the base and the CEDS cases, with different anthropogenic emission inventories. The anthropogenic emission inventory utilized in the base case simulation is CAMS-GLOB-ANT (v4.2, <https://eccad3.sedoo.fr>, abbreviated as “CAMS”), which contains 17 sectors with a spatial resolution of 0.1×0.1 degree and monthly temporal resolution. With the basic data of 2010 from the Emission Database for Global Atmospheric Research (EDGAR, v4.3.2), CAMS extends the period to recent years based on the trend factors derived



from the Community Emissions Data System (Hoesly et al., 2018). Meanwhile, Hoesly et al. (2018) pointed out that there are limitations in the system, especially in the emission trends for specific sectors, and emphasized the need for more detailed data to be incorporated into regional emission inventories. The other one used in the CEDS sensitivity simulation case for aerosol precursor emissions (NH_3 , SO_2 , and NO_x) is CEDS_GBD-MAPS (Mcduffie et al., 2020), abbreviated as “CEDS_GBD”. The CEDS_GBD is developed using the Community Emissions Data System and is reported as a function of 11 anthropogenic sectors and 4 fuel categories, with a spatial resolution of 0.5×0.5 degrees and monthly temporal resolution. Assuming that the specific regional emission inventories are more accurate, Mcduffie et al. (2020) updated the activity data and the core scaling procedure, modified the final emission gridding and aggregation procedures, and then utilized several regional emission inventories to improve the previous version of CEDS_GBD via the scaling procedure, which can not only reduce the discrepancy with other global emission inventories but also help to maintain the timeliness and regional accuracy of the global estimates. However, they also pointed out that the sources of uncertainty in the CEDS_GBD are similar to those in the CEDS.

Other NH_3 emissions include aircraft emissions from the CAMS-GLOB-AIR inventory (v1.1, <https://eccad3.sedoo.fr>), land and water biological emissions from the Global Emissions Inventory Activity (GEIA) inventory, and biomass burning emissions calculated by the BIOBURN submodel (Kaiser et al., 2012). BIOBURN determines the flux based on biomass burning emission factors and dry matter combustion rates from the Global Fire Assimilation System (GFAS), which calculates biomass burning emissions by assimilating Fire Radiative Power (FRP) observations from MODIS (Andreae, 2019).

2.1.2 Top-down scheme

The NH_3 emission inventory over land is updated by a top-down method with the constraint of IASI satellite observations (<https://iasi.aeris-data.fr>) developed by Luo et al. (2022). This fast top-down method updates the prior NH_3 emissions ($E_{\text{NH}_3, \text{mod}}$, molecule $\text{m}^{-2} \text{s}^{-1}$) with a correction term positively proportional to the biases between observed ($C_{\text{NH}_3, \text{obs}}$, molecule m^{-2}) and simulated ($C_{\text{NH}_3, \text{mod}}$, molecule m^{-2}) monthly averaged NH_3 total column densities and inversely proportional to the NH_3 lifetime ($\tau_{\text{NH}_3, \text{mod}}$, s) (Eq. 1). The $\tau_{\text{NH}_3, \text{mod}}$ is calculated as the ratio of the simulated NH_3 column and the sum of the simulated loss rate of the NH_x family ($\text{NH}_x \equiv \text{NH}_3 + \text{NH}_4^+$) through dry and wet deposition (Eq. 2).

$$E_{\text{NH}_3} = E_{\text{NH}_3, \text{mod}} + \frac{C_{\text{NH}_3, \text{obs}} - C_{\text{NH}_3, \text{mod}}}{\tau_{\text{NH}_3, \text{mod}}} \quad (1)$$

$$\tau_{\text{NH}_3, \text{mod}} = \frac{C_{\text{NH}_3, \text{mod}}}{D_{\text{NH}_3, \text{mod}} + D_{\text{NH}_4^+, \text{mod}}} \quad (2)$$

The fast top-down method relies on the total column concentrations retrieved by IASI. According to Damers et al. (2019), the dominant source of uncertainty in the IASI observational product stems from the systematic bias, with the negative bias estimated between 25% to 40%, compared to site observations (Damers et al., 2017). While this method simplifies the chemical and physical processes governing NH_3 , Luo et al. (2022) identified large uncertainties in regions like Central Asia and tropical Africa due to poorly constrained sources by IASI observations in these areas. Nonetheless, they demonstrated that simulations driven by the updated top-down emission inventory show better



215 consistency with satellite observations compared to those driven by the prior emission inventory.

2.1.3 Emission comparison

Overall, the global NH_3 emissions used in this study in all simulation cases range from 74 Tg yr^{-1} to 85 Tg yr^{-1} (Table 2), which is within the reported range of the current literature from 52 Tg yr^{-1} to 91 Tg yr^{-1} (Schlesinger and Hartley, 1992; Dentener and Crutzen, 1994; Bouwman et al., 1997; Olivier et al., 1998; Van Aardenne et al., 2001; 220 Bleeker et al., 2013). The distribution of the global NH_3 emission flux derived from the base case and the absolute emission flux difference between the sensitivity simulation cases and the base case are shown in Figure 1. Significant regional variations in NH_3 emission flux are found in Figure 1 (a), with the maximum emission flux exceeding $7 \text{ g m}^{-2} \text{ yr}^{-1}$ in northern India, eastern China, and central Europe, all regions with the highest population density. Other emission hotspots include the eastern United States, southeastern Latin America, and central and eastern Africa. The 225 base case is able to capture the global NH_3 emission hotspots reported by Van Damme et al. (2018). Meanwhile, the minimum flux below $0.01 \text{ g m}^{-2} \text{ yr}^{-1}$ is located in the Antarctic and Arctic regions and the Sahara Desert, as well as in remote oceans, where there is little impact from human activities. Agricultural activities including livestock and fertilization are the main source of NH_3 emissions in China, India, and the United States (Liu et al., 2022; Khan et al., 2020; Van Damme et al., 2018; Sahoo et al., 2024), while soil emissions, biomass burning and domestic fires are the main contributors to NH_3 emissions in central and eastern Africa (Hickman et al., 2021; Delon et al., 2012). 230

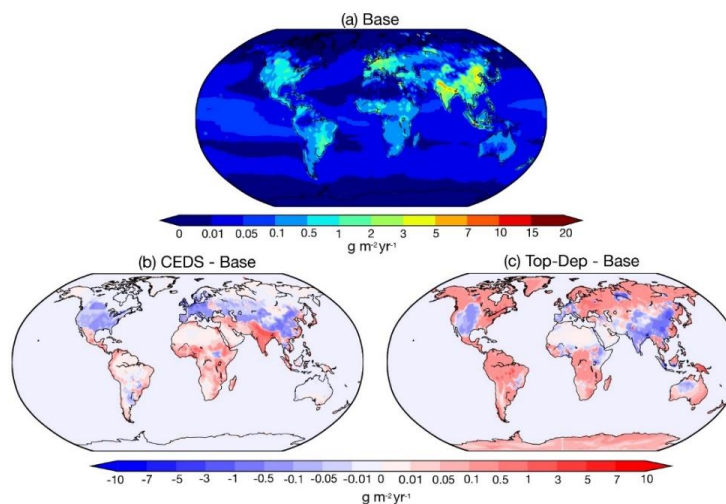


Figure 1. Global distribution of the annual average NH_3 emission flux for (a) the Base case and the absolute differences between (b) the Base and CEDS and (c) the Base and Top-Dep cases during 2010-2012.

235

Compared with the base case, both the CEDS and Top-Dep cases show an increase in the global NH_3 emission amount, with increases of 5% and 16%, respectively. The lower NH_3 emission fluxes of the CEDS case are found in North America, Europe, and China except for the northeastern and southeastern coastal areas, while emission fluxes are higher throughout India (Figure 1b). Slightly higher fluxes are also found in western and eastern Africa, the



northern Middle East, and southeastern Asia. According to McDuffie et al. (2020), the NH_3 emission flux from the Multi-resolution Emission Inventory for China (MEIC, <http://www.meicmodel.org>), European Monitoring and Evaluation Programme (EMEP), and US EPA are used to scale the previous emission (the basic data of 2010 from EDGAR) over mainland China, Europe, and the USA. The NH_3 emission flux from India and Africa remains the same as that of the original inventory. Constrained by the IASI satellite observation, the NH_3 emission flux of the Top-Dep case is increased in most regions of the world, but lower emission fluxes are estimated in regions such as western North America, western and southern Europe, India, China except the northeastern and southeastern coastal areas, and western Australia. The comparison of the absolute and relative difference between the base case and the other emission schemes is summarized in Table 2.

Table 2. Comparison of annual NH_3 emissions (Tg yr^{-1}) across global and regional scales between the two sensitivity cases and the base case.

Region	Base (Tg yr^{-1})	CEDS		Top-Dep	
		diff ^a	relative diff ^b (%)	diff ^a	relative diff ^b (%)
Globe	73.27	3.86	5.3	11.44	16
Land	61.14	3.05	5.0	11.26	18
North America	5.56	-1.00	-18	3.23	58
South America	8.20	0.69	8.4	4.18	51
Europe	6.44	-1.50	-23	1.01	16
Middle East	1.05	0.21	20	-0.01	-1.4
South Asia	10.11	3.79	38	-0.98	-9.7
East Asia	15.75	-2.03	-13	-2.58	-16

^a: absolute difference between sensitivity cases and the base case.

^b: relative difference between sensitivity cases and the base case.

2.2 ISORROPIA II

The thermodynamic equilibrium model ISORROPIA II is used to calculate the multi-phase mass transfer of the $\text{K}^+-\text{Ca}^{2+}-\text{Mg}^{2+}-\text{NH}_4^+-\text{Na}^+-\text{SO}_4^{2-}-\text{NO}_3^- -\text{Cl}^- -\text{H}_2\text{O}$ aerosol system (Nenes et al., 1998; Fountoukis and Nenes, 2007). The process of gas/aerosol partitioning is calculated in two steps (Pringle et al., 2010). In the first step, the amount of gas phase species kinetically able to condense on the aerosol within one timestep is calculated (Vignati et al., 2004). ISORROPIA II then re-distributes the mass between the gas and aerosol phase. In this study, ISORROPIA II runs in the forward mode with the input of relative humidity, temperature, and concentration of aerosol and gas phase species. ISORROPIA II determines the subsystem set of equilibrium equations and solves the equilibrium state by the chemical potential method. It outputs the equilibrium concentration of species in gas, solid, and liquid phases by assuming that the particle phase is in the thermodynamically stable-state mode where salts precipitate once the aqueous phase becomes saturated (Fountoukis and Nenes, 2007).

Meanwhile, a sensitivity case assuming the particle phase in the thermodynamically metastable state mode is performed with the same emission scheme as the base case. In the metastable state, the aerosol may be supersaturated with respect to dissolved salts and always consists only of an aqueous phase (Fountoukis and Nenes, 2007). Karydis et al. (2021) pointed out that more acidic particles (up to 2 pH units) are derived from the metastable assumption in regions affected by high concentrations of crustal cations and consistently low relative humidity values.

According to past studies, the treatment of crustal species (e.g. Ca^{2+} , K^+ , Mg^{2+}) in ISORROPIA II can improve model predictions (Karydis et al., 2010; Karydis et al., 2011), as both the phase partitioning of NO_3^- and the



thermodynamic interaction between NH_4^+ and the remaining ions in the aqueous phase are significantly affected. Karydis et al. (2016) found that when these crustal species are included in the EMAC model, the increase in global NO_3^- tropospheric load can be up to 44% while the global NH_4^+ tropospheric load decreases by 41%.

2.2.1 pH calculations

The pH is calculated from the negative decimal logarithm of the hydrogen ion activity,

$$\text{pH} = -\log_{10}(\gamma x_{\text{H}^+}) \quad (3)$$

where x_{H^+} and γ represent the molality of hydrogen ions in the solution and the ionic activity coefficient of hydrogen, respectively. With γ assumed to be unity, the pH value is derived using the hydrogen ion concentration in the aqueous particle phase output by ISORROPIA-II (in mol m^{-3}) and the aerosol water content output by GMXc (in mol mol^{-1}). Both hydrogen ion and aerosol water content are output every 5 hours, following Karydis et al. (2021). In addition, the temperature threshold of 269 K is set to ensure that the calculations are performed only when liquid water is present in the aerosol.

2.2.2 Two factors affecting pH value change

According to Equation (3), the pH value is determined by the concentrations of H^+ and H_2O . To evaluate the impact of each factor on the pH value, we independently calculate the changes in pH arising from two pathways: one driven by H^+ and the other by H_2O . The corresponding results are presented in Figures S16 and S17.

$$\Delta \text{pH}_{\text{H}_2\text{O}} = \log_{10} \frac{H_2\text{O} + \Delta H_2\text{O}}{H^+} - \log_{10} \frac{H_2\text{O}}{H^+} \quad (4)$$

$$\Delta \text{pH}_{\text{H}^+} = \log_{10} \frac{H_2\text{O}}{H^+ + \Delta H^+} - \log_{10} \frac{H_2\text{O}}{H^+} \quad (5)$$

Here, $\Delta \text{pH}_{\text{H}_2\text{O}}$ and $\Delta \text{pH}_{\text{H}^+}$ represent the changes in pH caused by variations in H_2O and H^+ concentrations, respectively. The base case concentrations of H_2O and H^+ are used as references, and the changes in concentration are expressed as $\Delta H_2\text{O}$ and ΔH^+ , corresponding to the deviations in H_2O and H^+ from their base case levels.

3. Observations

Multiple observational datasets are used in this study to validate the model simulation in different regions of the world as defined by the IPCC (2023). The information of each dataset is summarized in Table 3 and the site distribution is plotted in Figure 2 and Figure S1. These datasets include satellite retrievals from the Infrared Atmospheric Sounding Interferometer (IASI; https://iasi.aeris-data.fr/NH3_IASI_A_L3_data/), and observation site networks Nationwide Nitrogen Deposition Monitoring Network (NNDMN; https://figshare.com/articles/dataset/Data_Descriptor_Xu_et_al_20181211_Scientific_data_docx/7451357/5), the European Monitoring and Evaluation Programme (EMEP; <https://ebas-data.nilu.no/Default.aspx>), the Central Pollution Control Board (CPCB; <https://cpcb.nic.in/>), the Acid Deposition Monitoring Network in East Asia (EANET; <http://www.eanet.asia/product/index.html>), Ammonia Monitoring Network (AMoN;



<https://nadp.slh.wisc.edu/networks/ammonia-monitoring-network/>), the U.S. Environmental Protection Agency (EPA; <https://www.epa.gov/data>), and the Clean Air Status and Trends Network (CASTNET; <http://www.epa.gov/castnet>).

305

Table 3. Information for each observation dataset used to validate model simulation during 2010-2012.

Dataset	Parameters	Location
IASI	NH ₃ column concentration	Globe ^a
NNDMN	NH ₃ , NH ₄ ⁺ , NO ₃ ⁻ mass concentration	China (29 sites)
EMEP	NH ₃ , NH ₄ ⁺ , NO ₃ ⁻ , and SO ₄ ²⁻ mass concentration	Europe (25 sites for NH ₃ ; 7 sites of PM _{2.5} matrix ^b)
CPCB	NH ₃ mass concentration	India (8 sites)
EANET	NH ₄ ⁺ , NO ₃ ⁻ , and SO ₄ ²⁻ mass concentration	eastern and southeastern Asia (50 sites, PM _{2.5} matrix ^b)
AMoN	NH ₃ and NH ₄ ⁺ mass concentration	America (21 sites)
CASTNET	NH ₃ , NH ₄ ⁺ , NO ₃ ⁻ , and SO ₄ ²⁻ mass concentration	America (79 sites, PM _{2.5} matrix ^b)
EPA	NH ₄ ⁺ , NO ₃ ⁻ , and SO ₄ ²⁻ mass concentration	America (211 sites, PM _{2.5} matrix ^b)

^a: Only use the data over land.

^b: Measurements refer to a chemical or physical property of the total aerosol particle phase in the size fraction less than 2.5 micrometer median aerodynamic diameter.

310

Due to its better precision resulting from favorable thermal contrast conditions (Clarisse et al., 2009), only the morning (around 9:30 local time) overland IASI data is used in this study. The original temporal resolution of the various datasets includes hourly, three-day, daily, weekly, bi-weekly, and monthly, which we uniformly convert to monthly. The mean bias (MB), mean absolute gross error (MAGE), normalized mean bias (NMB), normalized mean error (NME), and root mean square error (RMSE) are calculated to evaluate the model performance:

315

$$MAGE = \frac{1}{N} \sum_{i=1}^N |P_i - O_i| \quad (6)$$

$$MB = \frac{1}{N} \sum_{i=1}^N (P_i - O_i) \quad (7)$$

$$NME = \frac{\sum_{i=1}^N |P_i - O_i|}{\sum_{i=1}^N O_i} \quad (8)$$

$$NMB = \frac{\sum_{i=1}^N (P_i - O_i)}{\sum_{i=1}^N O_i} \quad (9)$$

$$RMSE = \left[\frac{1}{N} \sum_{i=1}^N (P_i - O_i)^2 \right]^{\frac{1}{2}} \quad (10)$$

where P_i and O_i represent the monthly value of model simulation and measurement, respectively. N is the total number of data points used for comparison.

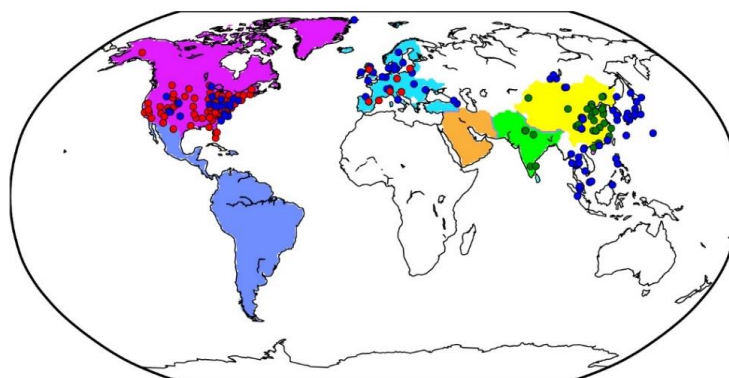


Figure 2. Regions and observation sites used in this study. North America, South America, Europe, Middle East, South Asia, and East Asia are marked by purple, navy blue, sky blue, orange, light green, and yellow, respectively. AMoN and CASTNET sites are represented by blue and red circles in North America (the EPA sites are shown in Figure S3). EMEP sites in Europe are shown by blue and red circles. CPCB sites are marked by green circles in South Asia, while NNDMN and EANET sites are indicated by dark green and dark blue in East Asia.

4. Observation evaluation

4.1 Aerosol comparison

The comparison between the simulation derived from the base case and the observational datasets is summarized in Tables 4 – 6. Compared with the NNDMN dataset, of which sites are mainly located in urban and rural areas of China, the base case overestimates the NH_3 mass concentration ($\text{NMB} = 0.19$), underestimates the NH_4^+ mass concentration ($\text{NMB} = -0.41$) though reproduces the NO_3^- mass concentration well ($\text{NMB} = -0.02$). Xie et al. (2022) summarized the NMB between observed NO_3^- and simulated values in China as ranging from -0.97 to 1.90 based on modelling studies in the last decade. The negligible bias of the simulated NO_3^- shows the good performance of the EMAC model in this region. However, the biases in the simulation of NH_3 and NH_4^+ indicate that the $\text{NH}_3/\text{NH}_4^+$ partitioning treatment is not efficient enough or over-simplified, as less NH_4^+ is produced even with sufficient NH_3 . Similarly, in Europe and North America, we obtain a positive bias of NH_3 mass concentration (EMEP dataset: $\text{NMB} = 2.26$; AMoN dataset: $\text{NMB} = 0.58$) and a comparably lower NH_4^+ mass concentration (EMEP dataset: $\text{NMB} = 0.05$; AMoN dataset: $\text{NMB} = -0.23$). On the other hand, the dry deposition of NH_3 in China is lower than reported from observations ($\text{NMB} = -0.28$; not shown), which contributes to a higher atmospheric NH_3 concentration.

Table 4. Comparison of the Base case predictions with monthly average observations from China and Europe during 2010–2012.

	NNDMN network Metric			EMEP network Metric			
	NH_3	NH_4^+	NO_3^-	NH_3	NH_4^+	NO_3^-	SO_4^{2-}
Observed ($\mu\text{g m}^{-3}$)	7.68	7.45	11.92	1.16	1.09	1.29	2.11
Simulated ($\mu\text{g m}^{-3}$)	9.14	4.40	11.70	3.79	1.15	3.33	1.24
MAGE ($\mu\text{g m}^{-3}$)	5.27	4.21	6.00	2.78	0.60	2.38	0.98
MB ($\mu\text{g m}^{-3}$)	1.46	-3.05	-0.22	2.63	0.06	2.04	-0.88
NME	0.69	0.56	0.50	2.40	0.55	1.84	0.46
NMB	0.19	-0.41	-0.02	2.26	0.05	1.58	-0.41
RMSE ($\mu\text{g m}^{-3}$)	7.43	6.55	9.07	4.03	0.97	2.95	1.63
Number of comparisons	765	765	765	832	249	320	320



345

Table 5. Comparison of the Base case predictions with monthly average observations from India and eastern Asia (PM₂₅ matrix) during 2010–2012.

	CPCB network Metric	EANET network Metric		
	NH ₃	NH ₄ ⁺	NO ₃ ⁻	SO ₄ ²⁻
Observed (μg m ⁻³)	30.07	0.84	1.22	2.95
Simulated (μg m ⁻³)	22.30	0.83	2.09	1.52
MAGE (μg m ⁻³)	21.25	0.55	1.58	1.74
MB (μg m ⁻³)	-7.78	-0.02	0.87	-1.43
NME	0.71	0.65	1.29	0.59
NMB	-0.26	-0.02	0.71	-0.49
RMSE (μg m ⁻³)	30.57	1.11	2.58	2.48
Number of comparisons	137	908	916	886

350

Table 6. Comparison of the Base case predictions with monthly average observations from America (PM₂₅ matrix) during 2010–2012.

	AMoN network Metric		CASTNET network Metric			EPA network Metric		
	NH ₃	NH ₄ ⁺	NH ₄ ⁺	NO ₃ ⁻	SO ₄ ²⁻	NH ₄ ⁺	NO ₃ ⁻	SO ₄ ²⁻
Observed (μg m ⁻³)	1.20	1.27	0.69	0.74	1.81	0.83	1.24	1.97
Simulated (μg m ⁻³)	1.89	0.99	0.90	1.96	1.34	1.02	2.22	1.44
MAGE (μg m ⁻³)	1.16	1.02	0.34	1.33	0.64	0.42	1.30	0.65
MB (μg m ⁻³)	0.69	-0.29	0.21	1.22	-0.46	0.19	0.98	-0.53
NME	0.97	0.80	0.49	1.80	0.36	0.51	1.05	0.33
NMB	0.58	-0.23	0.30	1.65	-0.26	0.23	0.79	-0.27
RMSE (μg m ⁻³)	1.64	1.43	0.45	1.71	0.86	0.60	1.76	0.90
Number of comparisons	553	552	2825	2825	2825	5085	5392	5429

355

In East and Southeast Asia, the mass concentration of NH₄⁺ is well reproduced (NMB = -0.02), while high and low discrepancies are found in the mass concentrations of NO₃⁻ and SO₄²⁻ (NMB = 0.71 and -0.49, respectively). Similar results were also found in Europe, with agreement for NH₄⁺ (NMB = 0.05) but an overestimation of the NO₃⁻ mass concentration (NMB = 1.58) and underestimated SO₄²⁻ (NMB = -0.41). The positive bias of the simulated NO₃⁻ is reported by many studies (Xie et al., 2022; Heald et al., 2012; Colette et al., 2011; Bian et al., 2017; Pozzer et al., 2022). The negative bias of SO₄²⁻ is considered a reason for the positive bias of NO₃⁻, regarding the thermodynamic equilibrium between NH₄⁺, SO₄²⁻, and NO₃⁻. The discrepancy in SO₄²⁻ and NO₃⁻ is also due to the missing heterogeneous oxidation reactions for SO₂ and NO_x in the model. Several studies have concluded that adding multiphase chemistry can significantly improve the model performance (Zheng et al., 2015; Zhang et al., 2021b). Cheng et al. (2016) and Zheng et al. (2024) pointed out that the multiphase reactions act as an important SO₄²⁻ source in haze pollution, while Guo et al. (2017a) argued that the multiphase reactions are not likely limited by the required alkaline environment.

360

365

In North America, the base case reproduces the mass concentration of SO₄²⁻ (NMB = -0.26), but overpredicts the mass concentrations of NH₄⁺ and NO₃⁻ (NMB = 0.23 and 0.79, respectively), which is in line with the findings of Walker et al. (2012). The excess NH₄⁺ promotes the formation of NO₃⁻, and the uncertain uptake coefficient of N₂O₅ used in models may contribute to more NO₃⁻ (Walker et al., 2012). The highest NH₃ mass concentration is found in India, especially in the Indo-Gangetic Plain. Our model basically captures the “hot spot”, with a slight negative bias (NMB = -0.26). However, the scarce observation sites and the lack of observed NH₄⁺, NO₃⁻ and SO₄²⁻ hinder further evaluation of the model performance.



370 4.2 pH value comparison

Due to the lack of direct measurement of aerosol acidity, we collect the $PM_{2.5}$ pH value from related studies to compare with our model simulation in Table 7. These pH values are calculated using the thermodynamic equilibrium model ISORROPIA or E-AIM with input from observational datasets. Compared with Guo et al. (2017b), our simulated pH value from the base case is higher in the western USA (4.3 vs 2.7), but the value from the Meta case is much closer (2.6). Both the base and Meta cases predict the same aerosol water content, and the high Ca^{2+} concentration from the Great Basin Desert leading to the precipitation of $CaSO_4$ is the main reason for the lower aerosol acidity in the base case (Karydis et al., 2021). It is worth noting that the effect of Ca^{2+} on aerosol acidity was not considered by Guo et al. (2017b). In Europe, although the good agreement between our simulated pH and the result of Guo et al. (2018) (both are 3.9) supports the model simulations, we note the overestimation of simulated alkaline species (sum of NH_4^+ and NH_3 , NMB = 17%) along with underestimation of acidic species (sum of NO_3^- and HNO_3 , NMB = -57%; SO_4^{2-} , NMB = -51%) in December emphasizes the improvement of the aerosol representation. In northern China, the pH value calculated by Wang et al. (2016) was more than 2 units higher (4.4 vs 6.7), and we suggest that the low bias is due to the underestimation of the mass concentration of cations (e.g. Ca^{2+} , Mg^{2+}) in $PM_{2.5}$, as the mass concentrations of NH_4^+ , SO_4^{2-} , and NO_3^- are in the observational ranges of Wang et al. (2016).

385

Table 7. Simulated pH value of $PM_{2.5}$ at single points compared with literature.

Location	Latitude	Longitude	Time Period	Method used	Field derived mean pH	Base	Meta	Reference
Egbert, ON, Canada	44.23	-79.78	Jul-Sep, 2012	E-AIM	2.1	3.77	1.57	Murphy et al. (2017)
Pasadena, CA, USA	34.14	-118.12	Jun, 2010	ISORROPIA	2.7	4.26	2.58	Guo et al. (2017)
Sao Paulo, Brazil	-23.55	-46.63	Aug-Sep, 2012	E-AIM	4.8	3.85	3.34	Vieira-Filho et al. (2016)
Cabauw, Netherlands	51.97	4.93	Dec-Feb, 2012	ISORROPIA	3.9	3.91	3.58	Guo et al. (2018)
Xi'an, China	34.23	108.89	Nov-Dec, 2012	ISORROPIA	6.7	4.41	3.20	Wang et al. (2016)

Note: table extracted in part from Karydis et al. (2021).

390 5. Secondary inorganic aerosol composition

5.1 Size-resolved composition

The regional mass fractions of size-resolved inorganic aerosol components (NH_4^+ , SO_4^{2-} , and NO_3^-) are presented as bar charts in Figure 3, while global distribution maps of their size-resolved mass concentrations are shown in Figure S2, both the simulation results are derived from base case. To assess ammonia neutralization of sulfuric and nitric acids, we applied the chemical domain framework defined by Ge et al. (2022) based on SNA molar concentrations in PM_{10} with a threshold of $>1 \mu g m^{-3}$. The four chemical domains, illustrated in Figure 4, are defined as follows: “ SO_4^{2-} very rich” ($totNH_3/totSO_4 < 1$, $totNH_3$: sum of NH_3 and NH_4^+ , $totSO_4$: sum of SO_4^{2-} and HSO_4^-), “ SO_4^{2-} rich” ($totNH_3/totSO_4$ between 1 and 2), “ NO_3^- rich” (free $NH_3/totNO_3$ between 0 and 1, free NH_3 : $totNH_3$ minus double $totSO_4$,



totNO₃: sum of NO₃⁻ and HNO₃), and “NH₃ very rich” (free NH₃/ totNO₃ > 1). Figure S3 shows the ratios used to
 400 define these domains.

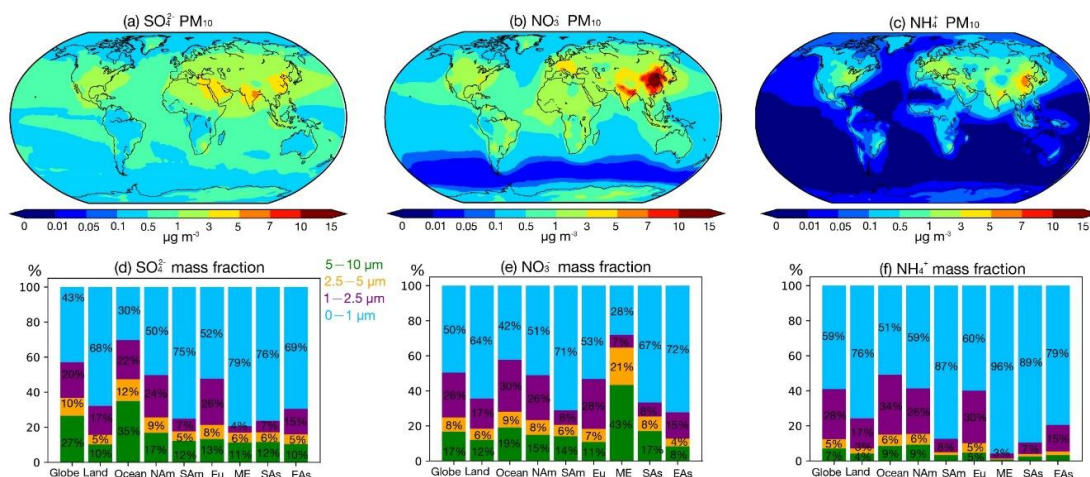


Figure 3. (a) – (c) global distribution of SO₄²⁻, NO₃⁻, and NH₄⁺ mass concentration in the size range of 0 – 10 µm, (d) – (f) bar
 plots for mean mass fractions of size-resolved NH₄⁺, SO₄²⁻, and NO₃⁻ over globe, land, ocean and regions (marked in Figure 2), the
 size range of 5 – 10 µm, 2.5– 5 µm, 1– 2.5 µm, and 0 – 1 µm are marked by green, orange, purple, and blue, respectively (NAM:
 405 North America; SAM: South America; Eu: Europe; ME: Middle East; SAs: South Asia; EAs: East Asia).

Regions with low inorganic aerosol concentrations (<1 µg m⁻³) are found in Southern Hemisphere oceans and
 remote areas such as the North Pole and South America, including the Amazon Basin. These areas represent relatively
 pristine baselines for evaluating anthropogenic impacts (Andreae et al., 1990; Andreae, 2007). In low northern latitude
 410 oceans, the “SO₄²⁻ very rich” and “SO₄²⁻ rich” domains dominate, characterized by NH₃ fully converted to NH₄⁺ but
 incomplete neutralization of sulfuric acid. This pattern reflects low NH₃ emissions over oceans (Figure 1) and the
 contribution of biogenic dimethyl sulfide (DMS) to marine SO₄²⁻ (Fiddes et al., 2018; Jackson et al., 2020). Additional
 NO_x and SO₂ from shipping contribute to marine SO₄²⁻ and NO₃⁻ (Wang et al., 2023; Burgard and Briä, 2016). Average
 PM₁₀ SNA concentrations are lower over oceans compared to land (NH₄⁺: 0.06 µg m⁻³ vs. 0.36 µg m⁻³; NO₃⁻: 0.37 µg
 415 m⁻³ vs. 1.24 µg m⁻³; SO₄²⁻: 0.60 µg m⁻³ vs. 0.95 µg m⁻³). Marine SO₄²⁻ and NO₃⁻ are predominantly in the super-micron
 mode, with mass fractions of 70% and 58%, respectively. Coastal areas exhibit a “NO₃⁻ rich” domain due to
 continental outflows (Figure S2) (Prospero et al., 1985), consistent with prior findings that marine aerosol in the super-
 micron mode primarily comprises inorganic salts, including sea salt, non-sea salt sulfate, and nitrate, while organic
 matter is concentrated in the sub-micron range (Russell et al., 2023; Cavalli et al., 2004).

420

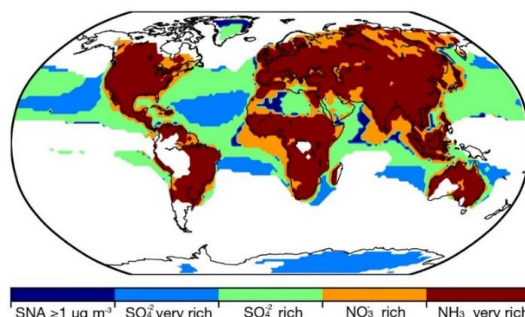


Figure 4. Distribution of ammonia neutralization state of sulfuric and nitric acids, based on SNA molar concentrations in PM₁₀ with a threshold of $\geq 1 \mu\text{g m}^{-3}$, where the SNA mass concentration less than the threshold is measured by blank zone. The “SO₄²⁻ very rich” represents the ratio of totNH₃ to totSO₄ less than 1 (totNH₃: sum of NH₃ and NH₄⁺, totSO₄: sum of SO₄²⁻ and HSO₄⁻), the “SO₄²⁻ rich” represents the ratio of totNH₃ to totSO₄²⁻ between 1 and 2, the “NO₃⁻ rich” represents the ratio of free NH₃ to totNO₃ between 0 and 1 (free NH₃: totNH₃ minus double totSO₄, totNO₃: sum of NO₃⁻ and HNO₃), and the “NH₃ very rich” represents the ratio of the free NH₃ to totNO₃ over 1.

On land, except for areas such as northern Russia, central Africa, and the Arabian Peninsula, the aerosol typically falls within the “NH₃ very rich” domain. In this domain, SO₄²⁻ is fully neutralized by NH₃, with sufficient NH₃ available to additionally neutralize NO₃⁻, making NO₃⁻ the limiting factor in NH₄NO₃ formation. More than 60% of SNA mass is in the sub-micron mode on land, while the super-micron modes (i.e. 1–2.5 μm , 2.5–5 μm and 5–10 μm) accounts for a smaller fraction (7% for NH₄⁺, 15% for SO₄²⁻, and 18% for NO₃⁻). In polluted regions such as East and South Asia, PM₁₀ SNA concentrations are three times higher than the global land average. For example, East Asia shows NH₄⁺: 1.88 $\mu\text{g m}^{-3}$, NO₃⁻: 5.31 $\mu\text{g m}^{-3}$, and SO₄²⁻: 2.29 $\mu\text{g m}^{-3}$, while South Asia records NH₄⁺: 1.58 $\mu\text{g m}^{-3}$, NO₃⁻: 3.68 $\mu\text{g m}^{-3}$, and SO₄²⁻: 3.18 $\mu\text{g m}^{-3}$. Free NH₃ is abundant in regions like southern North America, Europe, South Asia, and East Asia, with mean free NH₃/total NO₃⁻ ratios of 2.11, 3.77, 5.30, and 3.78, respectively. Over 75% of SNA mass in these regions is concentrated in the 0–1 μm and 1–2.5 μm size ranges. The NH₃ surplus reflects recent trends in precursor emissions, with stable or increasing NH₃ emissions contrasting with declining SO₂ and NO_x emissions (Zheng et al., 2018; Hand et al., 2012; Russell et al., 2012). In the Middle East, particularly the Arabian Peninsula, aerosol is dominated by desert dust with negligible NH₃ emissions. The “SO₄²⁻ rich” and “NO₃⁻ rich” domains predominate, where NH₃ levels are insufficient to neutralize acidic components fully, limiting NH₄NO₃ formation. Mean concentrations of NH₄⁺, NO₃⁻, and SO₄²⁻ in this region are 0.72 $\mu\text{g m}^{-3}$, 2.07 $\mu\text{g m}^{-3}$, and 3.19 $\mu\text{g m}^{-3}$, respectively. Over 70% of NO₃⁻ resides in the super-micron modes due to interactions with sea salt and crustal dust, which shift NO₃⁻ from sub-micron to super-micron modes (Chen et al., 2020; Koçak et al., 2007; Karydis et al., 2016). Sub-micron NH₄⁺ and SO₄²⁻ remain dominant, accounting for 96% and 79% of their respective fractions, consistent with Osipov et al. (2022), who identified anthropogenic sources as the primary contributors to fine particles in the region.

5.2 NH₃ column concentration

Figure 5 (a) shows the global distribution of NH₃ column concentration. The global area-weight mean value of NH₃ column concentration is 0.80 mg m⁻², with the highest value up to 30 mg m⁻² in the Indo-Gangetic Plain of India and the lowest value of less than 0.01 mg m⁻² in the remote oceans of the Southern Hemisphere and the South Pole.



Compared with previous studies that investigated NH_3 column concentrations based on satellite retrievals (Van Damme et al., 2014; Van Damme et al., 2015; Zhou et al., 2024), our results can capture the distribution of NH_3 hotspots worldwide, including the Indo-Gangetic Plain, the North China Plain, and West Africa and Amazonia, where biomass burning is dominant (Van Damme et al., 2018). However, Van Damme et al. (2018) pointed out that two-thirds of the NH_3 emission hotspots are underestimated by at least one order of magnitude in the NH_3 emission inventory EDGAR (CAMS-GLOB-ANT used in this study is derived from EDGAR, see 2.1.1). Given such an underestimation in the current NH_3 emission inventory, we further improve the emission by applying a new inventory and updating the current inventory using a top-down method introduced in Section 2.1. The simulation results are discussed in Section 7.

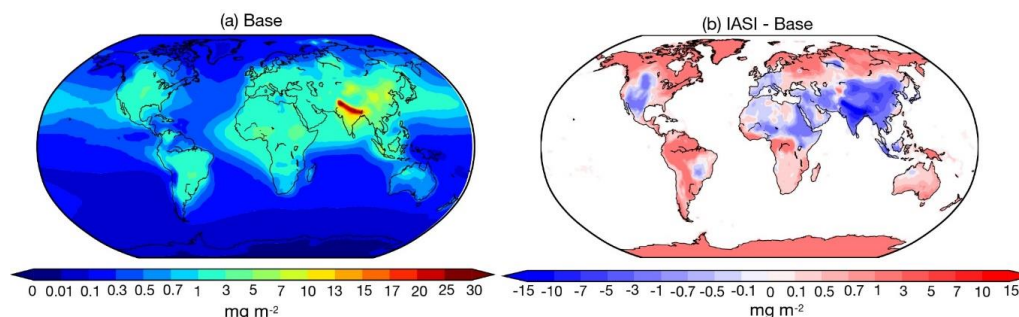


Figure 5. Global distribution of (a) the average NH_3 column concentration (mg m^{-2}) for the Base Case, and (b) the absolute difference between IASI satellite retrieval and Base case, from 2010 to 2012.

Our simulated NH_3 column concentrations show good agreement with the IASI satellite observations (Figure 5b), with global land mean values at a comparable level of 1.66 mg m^{-2} . However, regional biases can be significant, with an NMB of -0.32 . The model overestimates NH_3 column concentrations over regions such as India, China, western America, and northeastern Africa, while it has a negative bias in high-latitude regions. It is also important to note that biases in the IASI satellite products have been identified in previous studies (Dammers et al., 2017; Dammers et al., 2019), more details are discussed in Section 2.1.2.

5.3 Global NH_3 budget

The global budget for NH_3 and NH_4^+ is summarized in Table 8. Given a global NH_3 emission input of 74.37 Tg yr^{-1} , the global burden and lifetime derived from the base case simulation are 0.41 Tg and 2.01 days, respectively; for NH_4^+ , the global burden and lifetime are 0.34 Tg and 3.46 days, respectively. Based on the simulations of nine models, Bian et al. (2017) assessed that given the average NH_3 emission input of 76.38 Tg yr^{-1} , the average global burden and lifetime for NH_3 and NH_4^+ are 0.20 Tg and 0.72 days, and 0.32 Tg and 4.3 days, respectively. Compared to Bian et al. (2017), our study uses the same NH_3 emission input; however, the global burden and lifetime of NH_3 derived from the base case are larger. This potential overestimation may be attributed to the wet deposition scheme used in EMAC. The scavenging scheme (SCAV) accounts for pH adjustments in NH_3 dissolution. More specifically, the EMAC model implicitly determines the effective Henry's law constant by solving a system of coupled ordinary differential equations, explicitly representing liquid-phase processes in clouds and raindrops, including dissociation, acid-base



equilibria, redox reactions, and photolysis (Tost et al., 2006). This approach ensures a comprehensive calculation of total wet deposition for NH_4^+ and NH_3 . Notably, the NH_3 burdens simulated in the AeroCom model intercomparison by Bian et al. (2017) exhibit significant variability, spanning a factor of 17. This wide range underscores the sensitivity of atmospheric NH_4^+ and NH_3 burdens and lifetimes to model domain definitions, deposition pathways, and NH_3 chemical processes across different models (Ge et al., 2022).

Table 8. Atmospheric budget of NH_3 , NH_4^+ and NH_x ($\text{NH}_3 + \text{NH}_4^+$).

Simulation Case	Specie	Emission (Tg yr^{-1})	Burden (Tg)	Dry Deposition (Tg yr^{-1})	Wet Deposition (Tg yr^{-1})	Lifetime ^a (day)
Base	NH_3	73.27	0.41	28.22	-	2.01
CEDS		77.13	0.43	29.90	-	2.01
Top-Dep		84.71	0.41	34.36	-	1.77
Base	NH_4^+	-	0.34	1.16	34.69	3.46
CEDS		-	0.35	1.25	35.77	3.45
Top-Dep		-	0.35	1.52	36.19	3.39
Base	NH_x	-	0.75	29.38	34.69	3.68 (4.27) ^b
CEDS		-	0.78	31.15	35.77	3.66 (4.25)
Top-Dep		-	0.76	35.90	36.21	3.27 (3.85)

^a: NH_3 lifetime = Burden/Emission; NH_4^+ lifetime = Burden/(Dry Deposition + Wet Deposition);

^b: NH_x lifetime = NH_x Burden/ NH_3 Emission; in the parentheses, NH_x lifetime = NH_x Burden/ (Dry Deposition + Wet Deposition);

Considering the SCAV scavenging scheme, we further calculate the global budget for NH_x ($\text{NH}_3 + \text{NH}_4^+$) in Table 8. The global burden of NH_x is 0.75 Tg. Wet and dry deposition contribute almost equally to the sink accounting for 54% and 46%, respectively. The lifetime of NH_x is 3.68 – 4.27 days, depending on the calculation method. Ge et al. (2022) estimated a global budget for NH_x , with an input NH_3 emission of 64.48 Tg yr^{-1} . They calculated the global burden of NH_x to be 0.91 Tg, with a lifetime of 4.9–5.2 days and its wet and dry deposition contributing equally to the sink (i.e., 51% and 49% of total deposition, respectively).

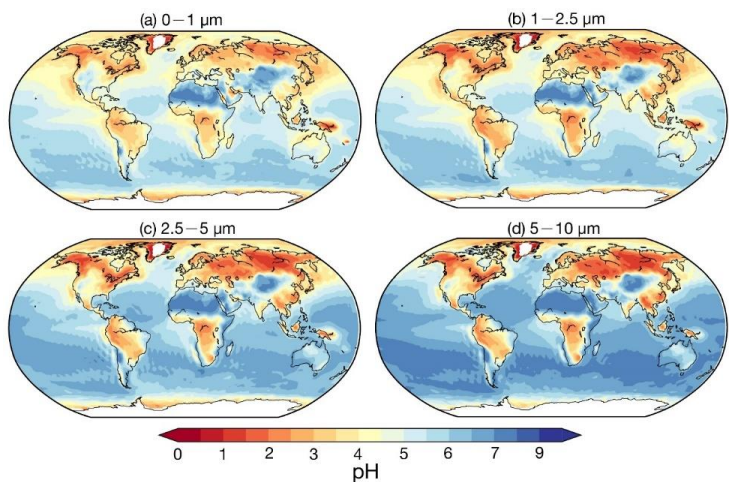
6. Aerosol acidity

Figure 6 illustrates the global distributions of size-resolved aerosol pH, with regional averages summarized in Table 9. Aerosol pH exhibits marked spatial variations, influenced by land-sea contrasts and regional sources. Over land in the Northern Hemisphere, excluding deserts, aerosols are generally acidic, whereas marine aerosols are alkaline due to sea salt influence. However, high-latitude marine aerosols are more acidic due to the low liquid water content and hydrogen ion outflow from land. The average pH values for land-based aerosols are 4.2 (5–10 μm), 4.2 (2.5–5 μm), 3.9 (1–2.5 μm), and 4.3 (0–1 μm). In contrast, marine aerosol pH values are 6.2 (5–10 μm), 5.8 (2.5–5 μm), 5.1 (1–2.5 μm), and 5.1 (0–1 μm). The deserts of North Africa, the Middle East, and the Gobi maintain the highest pH values (>7) across all size ranges, driven by non-volatile cations (e.g., Ca^{2+} , Mg^{2+}) that neutralize acidic components and enhance water uptake.

Regionally, higher pH values (5–5.7) in the Middle East are attributed to airborne dust, while coastal areas like the western Arabian Gulf have lower aerosol pH (<3 in 0–1 μm) due to elevated sulfate concentrations. In South Asia, abundant NH_3 emissions keep pH values between 5.4 and 4.9 despite high SO_2 and NO_x emissions. East Asia shows a distinct pH gradient, with desert regions in the northwest reaching pH >7 across all sizes, and southeast coastal areas exhibiting low pH (2–4), linked to significant SO_2 emissions and sulfate formation. Europe (pH 3.7–4.1) and North



515 America (pH 3.2–3.6) demonstrate moderate acidity, with the western USA exhibiting higher values (4–6) due to desert influences. In South America, pH ranges from 3.9 to 4.5, with coastal regions exceeding 6 due to sea salt.



520 **Figure 6.** Global distribution of surface average aerosol pH values in the size ranges: (a) 0 – 1 μm , (b) 1 – 2.5 μm , (c) 2.5 – 5 μm , (d) 5 – 10 μm , derived from Base case from 2010 to 2012.

An increasing trend in pH is observed from North America to Europe and East Asia, consistent with prior studies (Zhang et al., 2021a; Ding et al., 2019; Guo et al., 2017a). Aerosol alkalinity is driven by NH_4^+ and non-volatile cations, which neutralize SO_4^{2-} and NO_3^- , while water-soluble ions (WSIs) enhance liquid water uptake. East Asia exhibits the highest pH among regions, facilitated by relatively lower SO_4^{2-} , abundant NH_4^+ and WSIs, and significant NO_3^- and non-volatile cations in the coarse modes. These chemical properties outweigh the influence of meteorological effects such as differences in temperature and humidity.

Table 9. Size-resolved pH values across the globe and regions from simulation cases.

Region	0 – 1 μm			1 – 2.5 μm			2.5 – 5 μm			5 – 10 μm		
	Base ^a	Meta ^a	noNH ₃ ^a	Base ^a	Meta ^a	noNH ₃ ^a	Base ^a	Meta ^a	noNH ₃ ^a	Base ^a	Meta ^a	noNH ₃ ^a
Globe	4.9	4.19	3.28	4.83	4.3	4.09	5.38	5	4.82	5.75	5.47	5.46
Land	4.29	2.96	1.06	3.94	2.9	1.71	4.19	3.36	2.51	4.23	3.54	3.11
Ocean	5.1	4.58	3.99	5.11	4.75	4.86	5.76	5.52	5.56	6.24	6.08	6.21
North America	3.62	2.63	1.01	3.16	2.38	1.17	3.31	2.63	1.83	3.38	2.81	2.34
South America	4.11	3.25	1.46	3.85	3.26	2.26	4.4	4	3.25	4.52	4.22	3.84
Europe	4.09	2.97	0.84	3.65	2.8	1.27	3.69	2.92	1.91	3.75	3.08	2.67
Middle East	5.02	1.94	-0.17	5.25	2.08	0.51	5.47	3.59	1.86	5.66	4.18	3.85
South Asia	5.42	2.8	-0.2	4.86	2.33	0.43	5	2.73	1.37	5.04	2.88	2.16
East Asia	5.15	3.23	0.5	4.65	3.32	1.16	4.56	3.24	1.76	4.54	3.26	2.3

530 ^a: average pH value.



Contrary to previous findings (e.g. Kakavas et al., 2021; Ding et al., 2019), which suggest decreasing aerosol acidity with increasing particle size, pH in the base case (stable state) for 0–1 μm exceeds that of 1–2.5 μm over many regions, excluding oceans and the Middle East. This is examined through three perspectives. First, a sensitivity simulation (Meta case) assuming metastable conditions revealed lower pH across all sizes, with the greatest reductions in regions with high mineral cations and/or low relative humidity (RH), such as South Asia and the Middle East. In the metastable state, all anions remain aqueous, resulting in more acidic aerosols. While the Meta case explains some discrepancies, pH in the 0–1 μm size range remains higher relative to 1–2.5 μm in several regions (Table 5). Another sensitivity simulation, removing NH_3 emissions (no NH_3 case), significantly reduced pH across all sizes over land, especially in NH_3 -rich regions like South Asia and the Middle East, where 0–1 μm pH dropped below zero. This indicates increased pH sensitivity in the fine size ranges (i.e., 0–1 μm and 1–2.5 μm), particularly in regions where NH_3 availability is abundant. Excluding NH_3 , results in a consistent pH increase with particle size across all regions. Finally, a comparison with observed size-resolved mass concentrations from the EMEP network revealed an underestimation of acidic components (SO_4^{2-} and NO_3^-) and an overestimation of alkaline components in the 0–1 μm size range. This imbalance contributes to the anomalously high simulated pH in 0–1 μm . For instance, the observed SO_4^{2-} , NO_3^- and NH_4^+ in 0–1 μm accounts for 91%, 59% and 67% of 0–2.5 μm at the Montseny site (41.78 °N, 2.35° E) during 2010–2012 (observed NH_4^+ only available in 2010), respectively, compared to the accounting of 79%, 54% and 77% in simulation, highlighting a need for improved representation of aerosol composition in fine modes.

This study calculates size-resolved aerosol pH based on a log-normal size distribution, differing from other approaches. For instance, Kakavas et al. (2021) used the PMCAMx model, which employs a sectional approach to track aerosol mass and composition across 10 size bins ranging from 40 nm to 40 μm . The first five bins represent the PM_{10} fraction (0.04–1.25 μm), while three bins cover sizes up to 10 μm . In addition, previous studies on size-resolved aerosol acidity have certain limitations. For example, a laboratory study observed increasing aerosol acidity with decreasing particle size, but this trend only holds for pH below 2 (Craig et al., 2018). Similarly, a field study reached the same conclusion but lacked measurements of key gas-phase species (Fang et al., 2017).

7. Emission Sensitivity Analysis

The formation of secondary inorganic aerosols is strongly linked to NH_3 emissions (Wu et al., 2016; Chen et al., 2019; Liang et al., 2024). Xu et al. (2020) and Wang et al. (2015) have highlighted the critical role of gas-particle partitioning of $\text{NH}_3/\text{NH}_4^+$ in SNA formation, which is influenced by factors such as temperature, aerosol water content, and aerosol acidity (Nenes et al., 2020). Notably, the $\text{NH}_3/\text{NH}_4^+$ partitioning process buffers aerosol acidity, maintaining stability even amid shifts in acidic species like NO_3^- and SO_4^{2-} (Karydis et al., 2021). These findings suggest that the effects of NH_3 emissions on SNA formation and aerosol acidity remain a subject of debate (Weber et al., 2016; Zheng et al., 2022; Fu et al., 2017; Zou et al., 2024). However, most studies have focused on fine particles ($\text{PM}_{2.5}$ or PM_{10}), polluted regions (e.g., northern China), and haze episodes (Ge et al., 2019; Gao et al., 2016). Modeling studies often evaluate the effects of NH_3 emission changes by uniformly altering emission levels within each grid (Pozzer et al., 2017; Fu et al., 2017). While such approaches provide valuable insights, they may lack feasibility as NH_3 abundance correlates with population density, making uniform changes less representative of real-world



scenarios. To address this, we compare the effects of two NH_3 emission schemes CEDS and Top-Dep on size-resolved SNA mass concentration and aerosol acidity relative to a base case.

570 The NH_3 mass concentration serves as a proxy for NH_3 emissions, and differences in NH_3 mass concentrations between the scenarios and the base case (Figure S6) align with corresponding emission differences (Figure 1). Figures 7 and 8 show the responses of size-resolved NH_4^+ , NO_3^- , and SO_4^{2-} mass concentrations to NH_3 emission changes in the CEDS and Top-Dep cases, respectively. Similarly, Figure 9 illustrates the size-resolved aerosol acidity responses for the two cases. Additional details are provided in supplementary figures: Figures S7–S9 (CEDS case) and Figures 575 S11–S13 (Top-Dep case) depict the size-resolved responses of NH_4^+ , NO_3^- , and SO_4^{2-} mass concentrations, while Figures S10 and S14 highlight changes in size-resolved aerosol acidity.

The regional gas-particle partitioning ratios for $\text{NH}_3/\text{NH}_4^+$ ($\epsilon(\text{NH}_4^+) = \text{NH}_4^+ / (\text{NH}_4^+ + \text{NH}_3)$) and $\text{NO}_3^-/\text{HNO}_3$ ($\epsilon(\text{NO}_3^-) = \text{NO}_3^- / (\text{NO}_3^- + \text{HNO}_3)$) are shown in Figure S15. Regional emission amounts of NO_x and SO_2 from the CAMS and CEDS_GBD inventories are detailed in Table S1.

580 7.1 Size-Resolved SNA Response

Regarding the atmospheric budget of NH_3 (Table 8), a modest increase in global NH_3 emissions (CEDS case) slightly raises the burden and deposition of NH_3 and NH_4^+ , while the lifetime remains unchanged. In contrast, the larger emission increase in the Top-Dep cases does not alter the NH_3 burden but leads to higher deposition and a shorter lifetime for both species.

585

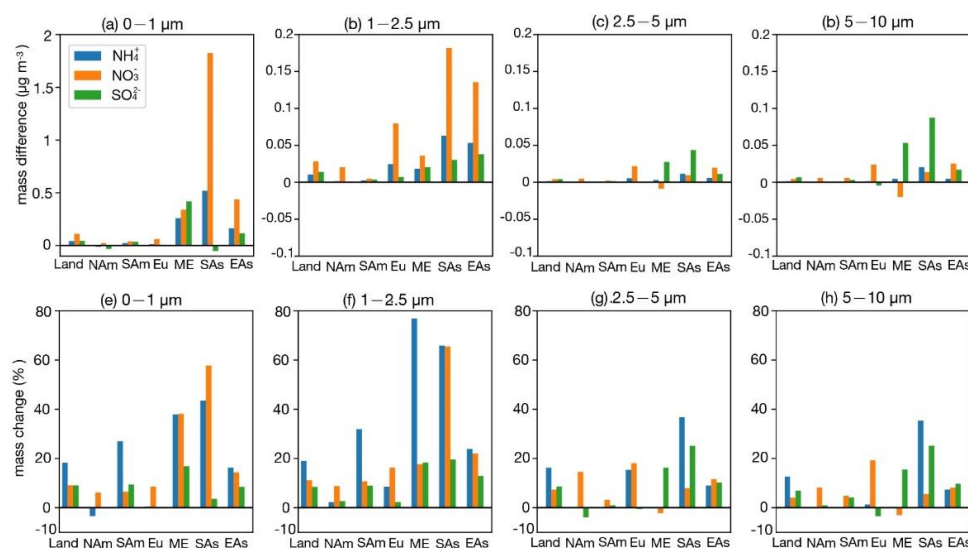


Figure 7. Bar plots for regional surface SNA mass concentration ($\mu\text{g m}^{-3}$) absolute difference between CEDS case and base case in the four size ranges (a) – (d); change ratio in the four size ranges (e) – (h). The calculation of change ratio in the size range of 0–1 μm is based on the mask of 0.1 $\mu\text{g m}^{-3}$, the change ratio in the size range of 1–2.5 μm , 2.5–5 μm and 5–10 μm is based on the mask of 0.05 $\mu\text{g m}^{-3}$ (Land: global land; NAm: North America; SAm: South America; Eu: Europe; ME: Middle East; SAs: South Asia; EAs: East Asia).

590



Across land regions, a small increase in NH_3 emissions (CEDS case), along with rising NO_x and SO_2 emissions, slightly raises $\epsilon(\text{NH}_4^+)$ while marginally lowering $\epsilon(\text{NO}_3^-)$ (Figure S15). The SNA mass concentration increases consistently across size ranges, with the most notable growth in NH_4^+ and NO_3^- in the 1–2.5 μm range (19% and 11%, respectively) and SO_4^{2-} in the submicron particles (9%). Under a larger NH_3 emission increase (Top-Dep case), $\epsilon(\text{NH}_4^+)$ drops significantly, and $\epsilon(\text{NO}_3^-)$ decreases slightly. The SNA response becomes more pronounced, with substantial increases in the 1–2.5 μm range (NH_4^+ : 104%, NO_3^- : 41%, SO_4^{2-} : 23%), while NO_3^- and SO_4^{2-} decrease in coarser particles. These shifts are linked to higher NH_3 emissions in relatively clean, high-latitude regions with low NH_3 flux (Figure 1c), which elevate NH_3 concentrations (Figure S6) enhancing NH_4^+ formation (Figure S11).

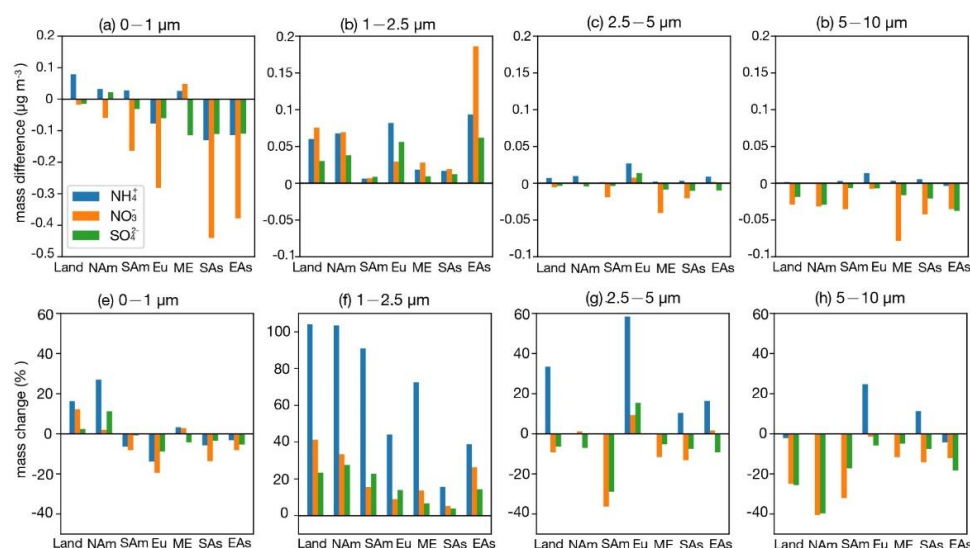


Figure 8. Bar plots for regional surface SNA mass concentration ($\mu\text{g m}^{-3}$) absolute difference between Top-Dep case and base case in the four size ranges (a) – (d); change ratio in the four size ranges (e) – (h). The calculation of change ratio in the size range of 0–1 μm is based on the mask of $0.1 \mu\text{g m}^{-3}$, the change ratio in the size range of 1–2.5 μm , 2.5–5 μm and 5–10 μm is based on the mask of $0.05 \mu\text{g m}^{-3}$ (Land: global land; NAm: North America; SAm: South America; Eu: Europe; ME: Middle East; SAs: South Asia; EAs: East Asia).

Regional analysis of SNA responses in Europe shows that a 23% reduction in NH_3 emissions, along with increases in NO_x and SO_2 emissions (CEDS case), raises $\epsilon(\text{NH}_4^+)$ slightly while causing a minor drop in $\epsilon(\text{NO}_3^-)$. The SNA mass increases mainly in the 1–2.5 μm range, with a slight decrease in SO_4^{2-} in coarser particles. Since Europe has abundant NH_3 , reductions are offset by existing availability and rising NO_x and SO_2 levels, leading to additional NH_4NO_3 and $(\text{NH}_4)_2\text{SO}_4$ formation. With higher NH_3 emissions (TopDep case), the response becomes more complex: SNA decreases in the submicron particles (Figure 8e) but increases in larger particles (Figure 8f–g), with the largest growth seen in NH_4^+ (~50%).

In East Asia, reducing NH_3 emissions while increasing NO_x and SO_2 emissions (CEDS case) raises $\epsilon(\text{NH}_4^+)$ and slightly increases $\epsilon(\text{NO}_3^-)$. SNA grows across all particle sizes, with the most significant changes in 1–2.5 μm range (Figure 7f). A similar NH_3 reduction in the Top-Dep case produces comparable $\epsilon(\text{NH}_4^+)$ and $\epsilon(\text{NO}_3^-)$ changes, with



SNA mainly decreasing in the submicron particles. The response in East Asia resembles that of Europe, where abundant NH_3 buffers SNA changes. In South Asia, NH_3 and NO_x emissions rise in the CEDS case while SO_2 emissions decline, slightly lowering $\epsilon(\text{NH}_4^+)$ and increasing $\epsilon(\text{NO}_3^-)$. NH_4^+ and NO_3^- concentrations grow across all size ranges (Figure 8), with the largest NH_4^+ increase found in 1–2.5 μm particles (66%) and NO_3^- rising in both submicron and 1–2.5 μm particles (~60%). SO_4^{2-} decreases in submicron particles but increases in coarser ones (25%). Conversely, reducing NH_3 emissions in the Top-Dep case raises $\epsilon(\text{NH}_4^+)$ and lowers $\epsilon(\text{NO}_3^-)$, leading to SNA declines, especially in submicron particles. South Asia, with abundant NH_3 , shows NO_3^- as the limiting factor for NH_4NO_3 formation, driving strong $\epsilon(\text{NO}_3^-)$ and NO_3^- responses in finer particles.

In North America, NH_3 and SO_2 emissions decrease, while NO_x emissions slightly rise (CEDS case). $\epsilon(\text{NH}_4^+)$ increases marginally, whereas $\epsilon(\text{NO}_3^-)$ declines slightly. NH_4^+ and SO_4^{2-} show minor reductions in submicron particles, while NO_3^- increases. In the Top-Dep case, a sharp rise in NH_3 emissions, mainly over Canada and Greenland, significantly lowers $\epsilon(\text{NH}_4^+)$, stabilizes $\epsilon(\text{NO}_3^-)$, and increases NH_4^+ and SO_4^{2-} in 1–2.5 μm particles. In South America, a small NH_3 emission rise (CEDS case) has little effect on $\epsilon(\text{NH}_4^+)$ or $\epsilon(\text{NO}_3^-)$, resulting in minimal aerosol composition changes. However, a substantial NH_3 increase (Top-Dep case) significantly boosts NH_3 concentrations, reduces $\epsilon(\text{NH}_4^+)$ and $\epsilon(\text{NO}_3^-)$, and shifts aerosol partitioning to smaller particles, particularly in central regions. Decreased NO_3^- and SO_4^{2-} in surrounding areas (Figures S12–13) suggest NH_3 is neutralizing transported species, explaining the observed $\epsilon(\text{NO}_3^-)$ reduction. Changes in other particle size ranges are minimal. In the Middle East, NH_3 emissions rise moderately (20%), along with slight NO_x and SO_2 increases (CEDS case). $\epsilon(\text{NH}_4^+)$ and $\epsilon(\text{NO}_3^-)$ remain stable, with NH_4^+ and NO_3^- increasing mainly in submicron particles (~40%), while SO_4^{2-} grows across sizes (~15%). A minor NH_3 emission drop (Top-Dep case) reduces NH_3 concentrations but enhances SNA in 1–2.5 μm particles, highlighting compensatory NH_3 effects in "NH₃ very rich" domains.

Overall, higher NH_3 emissions enhance SNA formation, particularly in the fine size ranges (0–1 μm and 1–2.5 μm). Greater NH_4^+ formation (e.g., Top-Dep case) depletes NO_3^- and SO_4^{2-} from coarse size ranges, leading to decreases in 2.5–5 μm and 5–10 μm . In low-SNA regions (e.g., South America, Greenland), NH_3 increases have limited SNA impacts but substantially elevate NH_3 concentrations. In "NH₃ very rich" regions (e.g., East Asia, Europe), NH_3 reductions alone may still increase $\epsilon(\text{NH}_4^+)$, promoting further SNA formation. These findings align with Zou et al. (2024), emphasizing the greater effectiveness of NO_x reductions in $\text{PM}_{2.5}$ mitigation compared to NH_3 or SO_2 control in ammonia-rich environments. Coordinated control of precursor emissions is crucial for mitigating air pollution, especially in heavily polluted regions (Wen et al., 2024).

7.2 Aerosol acidity response

7.2.1 Size-resolved pH changes

Among atmospheric buffering agents (e.g., conjugate acid-base pairs like $\text{NH}_3/\text{NH}_4^+$ and $\text{CO}_2/\text{HCO}_3^-$, as well as organic acids), the $\text{NH}_3/\text{NH}_4^+$ acid-base pair exhibits the largest buffering capacity for aerosols, dominating much of the continental urban areas (Zheng et al., 2023; Zheng et al., 2020). When NH_3 emissions are entirely eliminated, changes in oceanic pH values are negligible compared to the base case (no NH_3 case, Table 5 and Figure S5). However, aerosols over land become significantly more acidic, with pH values in the 0–1 μm size range dropping to -0.2 in



South Asia and -0.17 in the Middle East. The most substantial pH decreases occur in 0–1 μm aerosols, primarily in South Asia, East Asia, Europe, North America, and South America, consistent with the “ NH_3 -buffered regions” identified by Zheng et al. (2020).

Interestingly, while neither the Middle East nor northern Africa are categorized as “ NH_3 -buffered regions,” noticeable pH decreases are observed in the 0–1 μm and 1–2.5 μm size ranges over the Middle East, including Egypt and Libya. In these regions, the SNA is dominated by “ SO_4^{2-} rich” and “ NO_3^- rich” chemical domains (Figure 4), where NH_4^+ cannot fully neutralize the available NO_3^- and SO_4^{2-} . This results in excess acidic components, particularly in the 0–1 μm and 1–2.5 μm size ranges (Figure S2). Without NH_3 emissions, the abundance of NO_3^- and SO_4^{2-} further increases aerosol acidity.

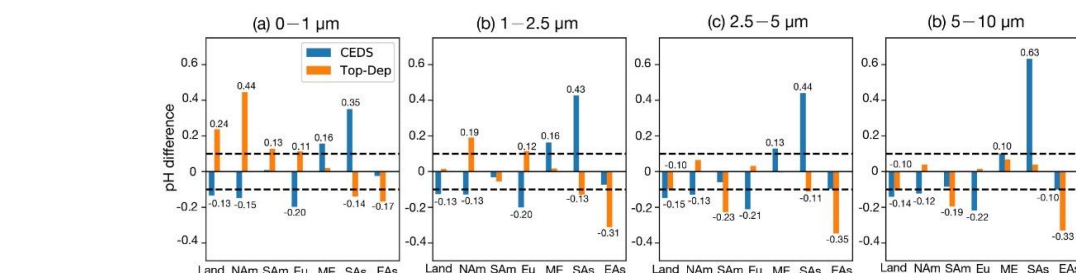


Figure 9. Bar plots for pH value absolute difference between CEDS/Top-Dep case and base case in the four size ranges (a)–(d), with the two dashed lines representing the value of 0.1 and -0.1, respectively (Land: global land; NAm: North America; SAM: South America; Eu: Europe; ME: Middle East; SAs: South Asia; EAs: East Asia).

Compared to the base case, size-resolved pH values in the CEDS case show an average decrease of -0.13 to -0.15 units over land. The most pronounced decreases occur in remote regions of the Northern Hemisphere (Figure S10), where NH_3 emission flux is relatively low. In contrast, the Top-Dep case exhibits an average pH increase of 0.24 units in the 0–1 μm range over land, driven by the higher NH_3 emission flux. This NH_3 -driven alkalization effect is less pronounced in the 1–2.5 μm range due to counteracting acidification effects from newly formed acidic components, as suggested by Zheng et al. (2024). Notably, pH decreases of -0.10 units are found in the 2.5–5 μm and 5–10 μm size ranges.

In East Asia, the pH changes in the CEDS case are concentrated in the 2.5–5 μm and 5–10 μm ranges (-0.10 units in both), with minimal changes in 0–1 μm and 1–2.5 μm . In the Top-Dep case, however, pH changes are more drastic across all size ranges: 0–1 μm (-0.17 units), 1–2.5 μm (-0.31 units), 2.5–5 μm (-0.35 units), and 5–10 μm (-0.33 units). These discrepancies between cases highlight that a reduction in NH_3 emissions enhances aerosol acidity (as in the Top-Dep case), but this effect can be partially offset by shifts in SO_4^{2-} and NO_3^- mass concentrations (as in the CEDS case). For instance, in the CEDS case, decreases in SO_4^{2-} and NO_3^- concentrations result in pH rises of 0.15–0.25 units across all size ranges compared to the Top-Dep case.

Our simulation results align with other studies. For example, Song et al. (2019) found that a ~ 0.3 increase in $\log_{10}[\text{NH}_3]$ contributed to a 0.3–0.4 unit rise in PM_{10} pH in Beijing during winter between 2014/2015 and 2018/2019. Concurrent changes in aerosol composition (increased NO_3^- and reduced SO_4^{2-} and Cl^-) led to a modest 0.1 units pH



increase. Similarly, Zhou et al. (2022) observed a minor $\text{PM}_{2.5}$ pH decrease of -0.24 units in the Yangtze River Delta region from 2011 to 2019, despite significant changes in aerosol composition resulting from the Air Pollution Prevention and Control Action Plan.

690 7.2.2 Drivers of pH Changes

We further quantify the changes in pH values between the CEDS/Top-Dep cases and the base case, isolating the contributions from changes in H^+ and H_2O concentrations (detailed in Section 2.2.2). The results are presented in Figures S16 and S17.

695 In the CEDS case, the decreased pH values across all four aerosol size ranges are primarily driven by changes in H^+ concentrations, particularly over the remote regions of the Northern Hemisphere. The effects of H_2O concentration changes are particularly relevant in the Middle East and South Asia. Notably, a substantial pH increase is observed in South Asia, with increases of 0.35, 0.43, 0.44, and 0.63 units in the 0–1 μm , 1–2.5 μm , 2.5–5 μm , and 5–10 μm size ranges, respectively. These increases are predominantly caused by changes in H^+ concentrations, which fully counteract the pH-decreasing effects of changes in H_2O concentrations.

700 In the Top-Dep case, although changes in H^+ concentrations significantly enhance pH values in the 0–1 μm size range, the pH-decreasing effects of changes in H_2O concentrations are distributed across all four size ranges over the entire land surface. In East Asia, both H^+ and H_2O concentration changes contribute substantially to the observed pH decreases, highlighting their combined impact.

705 In summary, NH_3 emissions play a crucial role in maintaining terrestrial aerosols at moderately acidic levels, particularly in the fine-mode size range of 0–1 μm . When NH_3 emissions are completely removed in the model, the largest pH decreases are found in this size range. Our findings underscore that, in the fine-mode ranges (0–1 μm and 1–2.5 μm), pH changes closely correspond to variations in NH_3 emissions, reflecting the distinct sensitivity of size-resolved pH to NH_3 levels. In the coarser size ranges (2.5–5 μm and 5–10 μm), however, pH changes are governed by the competing influences of H^+ and H_2O concentration changes.

710 8. Conclusion

This study applied three distinct ammonia (NH_3) emission schemes to the global atmospheric chemistry and climate model (EMAC) to assess the impact of NH_3 emissions on the size-resolved sulfate-nitrate-ammonium (SNA) aerosol composition and aerosol acidity. The emission schemes included two bottom-up inventories, and one inventory updated through a top-down approach. By simulating the size ranges of 0–1 μm , 1–2.5 μm , 2.5–5 μm , and 5–10 μm , 715 the study provides a comprehensive analysis of the role of NH_3 emissions in influencing global aerosol composition and acidity.

The model accurately captures the distribution of global NH_3 hotspots, but comparisons with observational datasets reveal positive biases in NH_3 concentrations and underestimations of NH_4^+ in regions such as China, North America, and Europe. This discrepancy suggests inefficiencies or oversimplifications in the $\text{NH}_3/\text{NH}_4^+$ partitioning treatment, 720 with insufficient NH_4^+ generated despite NH_3 availability. In East and Southeast Asia, NH_4^+ concentrations are well-simulated, but significant discrepancies were found for NO_3^- and SO_4^{2-} , likely due to the absence of heterogeneous



oxidation processes in the model. The simulated global NH_3 burden and lifetime are higher than reported in related studies, attributed to the wet deposition scheme used in EMAC which accounts for pH adjustments for NH_3 dissolution.

725 Over oceans, NH_3 is entirely converted to NH_4^+ , while SO_4^{2-} remains partially neutralized due to low NH_3 emissions and high SO_4^{2-} levels from biogenic dimethyl sulfide (DMS) emissions and NO_x and SO_2 from shipping. Marine SO_4^{2-} and NO_3^- are dominant in the super-micron modes, with mass fractions of 70% and 58%, respectively. On land, SO_4^{2-} is generally fully neutralized by NH_3 , except in regions such as northern Russia, central Africa, and the Arabian Peninsula. Terrestrial NO_3^- is also largely neutralized by NH_3 , resulting in over 60% of SNA concentrated in
 730 the sub-micron mode. In polluted areas such as East and South Asia, sub-micron SNA fractions exceed 70%, with South Asia exhibiting nearly 90% sub-micron NH_4^+ . In contrast, the Middle East, dominated by dust and with minor NH_3 emissions, shows incomplete neutralization of SO_4^{2-} and NO_3^- . Here, nearly 70% of NO_3^- resides in the super-micron modes, while NH_4^+ and SO_4^{2-} dominate the sub-micron mode with respective mass fractions of 96% and 79%.

In the Northern Hemisphere, terrestrial aerosols are generally more acidic than marine aerosols, except in desert
 735 regions. Remote marine and desert aerosols remain neutral due to the alkaline influence of sea salt and non-volatile cations in dust, which enhance water uptake and neutralize SO_4^{2-} and NO_3^- . However, at high latitudes, marine aerosols become more acidic due to the long-range transport of anthropogenic pollutants from continental sources. The 0–1 μm size range exhibits higher pH values than the 1–2.5 μm range in many regions, a trend influenced by several factors. These include the assumption of a thermodynamically stable aerosol phase in the ISORROPIA model,
 740 the high sensitivity of aerosol acidity to NH_3 in the 0–1 μm range and observed lower concentrations of acidic components (SO_4^{2-} and NO_3^-) in this size range compared to larger sizes.

An 18% increase in NH_3 emissions over land leads to a significant increase in SNA concentrations in the 1–2.5 μm size range (NH_4^+ : 104%, NO_3^- : 41%, SO_4^{2-} : 23%), while coarse mode SNA (2.5–10 μm) decreases. However, changes in size-resolved pH remain minimal, with the largest increase of 0.24 pH units occurring in the 0–1 μm range. In
 745 regions with low SNA, such as South America and Greenland, increased NH_3 emissions only lead to higher NH_3 concentrations due to the limited availability of HNO_3 and H_2SO_4 for SNA formation. Conversely, in NH_3 -rich regions such as East Asia and Europe, reductions in NH_3 emissions trigger compensatory effects, as excess NH_3 and available SO_2 and NO_x help to maintain SNA formation despite the reduced NH_3 supply. The buffering effect of NH_3 plays a crucial role in stabilizing aerosol acidity in densely populated areas, mitigating the effects of fluctuations in precursor
 750 gases.

In summary, this study underscores the critical influence of NH_3 emissions on global aerosol composition and acidity, with pronounced impacts on the size-resolved composition and properties of SNA aerosols. NH_3 emissions significantly modulate aerosol acidity, particularly in sub-micron ranges, highlighting the sensitivity of fine-mode aerosols to NH_3 levels. By buffering changes in aerosol pH, NH_3 emissions contribute to maintaining a relatively
 755 stable aerosol acidity, especially in heavily populated and industrialized regions. These findings emphasize the importance of accurately representing NH_3 dynamics in models for predicting atmospheric chemistry and climate interactions.



760 Code and Data Availability

The usage of MESSy (Modular Earth Submodel System) and access to the source code is licensed to all affiliates of institutions which are members of the MESSy Consortium. Institutions can become a member of the MESSy Consortium by signing the “MESSy Memorandum of Understanding”. More information can be found on the MESSy Consortium website: <http://www.messy-interface.org> (last access: 31 January 2025). The code used in this study has been based on MESSy version 2.55 and is archived with a restricted access DOI (<https://doi.org/10.5281/zenodo.8379120>, The MESSy Consortium, 2023). The data produced in the study is available from the authors upon request.

Acknowledgements

The work described in this paper has received funding from the Initiative and Networking Fund of the Helmholtz Association through the project “Advanced Earth System Modelling Capacity (ESM)”. The authors gratefully acknowledge the Earth System Modelling Project (ESM) for funding this work by providing computing time on the ESM partition of the supercomputer JUWELS (Alvarez, 2021) at the Jülich Supercomputing Centre (JSC). Xurong Wang has been supported by the China Scholarship Council (CSC).

Competing Interests

At least one of the (co-)authors is a member of the editorial board of Atmospheric Chemistry and Physics.

Author Contributions

XW and VAK planned the research and wrote the manuscript. XW performed the simulations and analyzed the results, assisted by VAK and APT. XW and APT collected the observational data and conducted the model evaluation. XW and ZL designed the Top-Dep case. All the authors discussed the results and contributed to the paper.

780 Reference

- Aas, W., Mortier, A., Bowersox, V., Cherian, R., Faluvegi, G., Fagerli, H., Hand, J., Klimont, Z., Galy-Lacaux, C., Lehmann, C. M. B., Myhre, C. L., Myhre, G., Olivie, D., Sato, K., Quaas, J., Rao, P. S. P., Schulz, M., Shindell, D., Skeie, R. B., Stein, A., Takemura, T., Tsyro, S., Vet, R., and Xu, X.: Global and regional trends of atmospheric sulfur, *Scientific Reports*, 9, 953, 10.1038/s41598-018-37304-0, 2019.
- 785 Alexander, L., Allen, S., Bindoff, N., Breon, F.-M., Church, J., Cubasch, U., Emori, S., Forster, P., Friedlingstein, P., Gillett, N., Gregory, J., Hartmann, D., Jansen, E., Kirtman, B., Knutti, R., Kanikicharla, K., Lemke, P., Marotzke, J., Masson-Delmotte, V., and Xie, S.-P.: Climate change 2013: The physical science basis, in contribution of Working Group I (WGI) to the Fifth Assessment Report (AR5) of the Intergovernmental Panel on Climate Change (IPCC), in, 2013.
- 790 Allen, H. M., Draper, D. C., Ayres, B. R., Ault, A., Bondy, A., Takahama, S., Modini, R. L., Baumann, K., Edgerton, E., Knote, C., Laskin, A., Wang, B., and Fry, J. L.: Influence of crustal dust and sea spray supermicron particle concentrations and acidity on inorganic NO₃⁻ aerosol during the 2013 Southern Oxidant and Aerosol Study, *Atmos. Chem. Phys.*, 15, 10669-10685, 10.5194/acp-15-10669-2015, 2015.
- 795 Andreae, M., Berresheim, H., Bingemer, H., Jacob, D. J., Lewis, B., Li, S. M., and Talbot, R. W.: The atmospheric sulfur cycle over the Amazon Basin: 2. Wet season, *Journal of Geophysical Research: Atmospheres*, 95, 16813-16824, 1990.
- Andreae, M. O.: Aerosols Before Pollution, *Science*, 315, 50-51, doi:10.1126/science.1136529, 2007.
- Andreae, M. O.: Emission of trace gases and aerosols from biomass burning – an updated assessment, *Atmos. Chem. Phys.*, 19, 8523-8546, 10.5194/acp-19-8523-2019, 2019.
- 800 Astitha, M., Lelieveld, J., Abdel Kader, M., Pozzer, A., and de Meij, A.: Parameterization of dust emissions in the



- global atmospheric chemistry-climate model EMAC: impact of nudging and soil properties, *Atmos. Chem. Phys.*, 12, 11057-11083, 10.5194/acp-12-11057-2012, 2012.
- 805 Bacer, S., Sullivan, S. C., Karydis, V. A., Barahona, D., Krämer, M., Nenes, A., Tost, H., Tsimpidi, A. P., Lelieveld, J., and Pozzer, A.: Implementation of a comprehensive ice crystal formation parameterization for cirrus and mixed-phase clouds in the EMAC model (based on MESSy 2.53), *Geosci. Model Dev.*, 11, 4021-4041, 10.5194/gmd-11-4021-2018, 2018.
- Beusen, A. H. W., Bouwman, A. F., Heuberger, P. S. C., Van Drecht, G., and Van Der Hoek, K. W.: Bottom-up uncertainty estimates of global ammonia emissions from global agricultural production systems, *Atmospheric Environment*, 42, 6067-6077, <https://doi.org/10.1016/j.atmosenv.2008.03.044>, 2008.
- 810 Bian, H., Chin, M., Hauglustaine, D. A., Schulz, M., Myhre, G., Bauer, S. E., Lund, M. T., Karydis, V. A., Kucsera, T. L., Pan, X., Pozzer, A., Skeie, R. B., Steenrod, S. D., Sudo, K., Tsigaridis, K., Tsimpidi, A. P., and Tsyro, S. G.: Investigation of global particulate nitrate from the AeroCom phase III experiment, *Atmos. Chem. Phys.*, 17, 12911-12940, 10.5194/acp-17-12911-2017, 2017.
- 815 Bleeker, A., Vries, W. d., Dentener, F., Sutton, M. A., Reis, S., Riddick, S. N., Dragosits, U., Nemitz, E., Theobald, M. R., Tang, Y. S., Braban, C. F., Viena, M., Dore, A. J., Mitchell, R. F., Wanless, S., Daunt, F., Fowler, D., Blackall, T. D., Milford, C., Flechard, C. R., Loubet, B., Massad, R., Cellier, P., Coheur, P. F., Clarisse, L., Damme, M. v., Ngadi, Y., Clerbaux, C., Ambelas Skjoth, C., Geels, C., Hertel, O., Wichink Kruit, R. J., Pinder, R. W., Bash, J. O., Walker, J. D., Simpson, D., Horvath, L., and Misselbrook, T. H.: Towards a climate-dependent paradigm of ammonia emission and deposition, urn:NBN:nl:ui:24-uuid:1516f098-ca7e-402b-a05d-83633f8c2612, 2013.
- 820 Bougiatioti, A., Nikolaou, P., Stavroulas, I., Kouvarakis, G., Weber, R., Nenes, A., Kanakidou, M., and Mihalopoulos, N.: Particle water and pH in the eastern Mediterranean: source variability and implications for nutrient availability, *Atmos. Chem. Phys.*, 16, 4579-4591, 10.5194/acp-16-4579-2016, 2016.
- Bouwman, A. F., Boumans, L. J. M., and Batjes, N. H.: Estimation of global NH₃ volatilization loss from synthetic fertilizers and animal manure applied to arable lands and grasslands, *Global Biogeochemical Cycles*, 16, 8-1-8-14, <https://doi.org/10.1029/2000GB001389>, 2002.
- 825 Bouwman, A. F., Lee, D. S., Asman, W. A. H., Dentener, F. J., Van Der Hoek, K. W., and Olivier, J. G. J.: A global high-resolution emission inventory for ammonia, *Global Biogeochemical Cycles*, 11, 561-587, <https://doi.org/10.1029/97GB02266>, 1997.
- Burgard, D. A. and Bria, C. R. M.: Bridge-based sensing of NO_x and SO₂ emissions from ocean-going ships, *Atmospheric Environment*, 136, 54-60, <https://doi.org/10.1016/j.atmosenv.2016.04.014>, 2016.
- 830 Cai, S., Wang, Y., Zhao, B., Wang, S., Chang, X., and Hao, J.: The impact of the "Air Pollution Prevention and Control Action Plan" on PM_{2.5} concentrations in Jing-Jin-Ji region during 2012–2020, *Science of The Total Environment*, 580, 197-209, <https://doi.org/10.1016/j.scitotenv.2016.11.188>, 2017.
- 835 Cavalli, F., Facchini, M. C., Decesari, S., Mircea, M., Emblico, L., Fuzzi, S., Ceburnis, D., Yoon, Y. J., O'Dowd, C. D., Putaud, J.-P., and Dell'Acqua, A.: Advances in characterization of size-resolved organic matter in marine aerosol over the North Atlantic, *Journal of Geophysical Research: Atmospheres*, 109, <https://doi.org/10.1029/2004JD005137>, 2004.
- Chang, Y., Zou, Z., Zhang, Y., Deng, C., Hu, J., Shi, Z., Dore, A. J., and Collett, J. L., Jr.: Assessing Contributions of Agricultural and Nonagricultural Emissions to Atmospheric Ammonia in a Chinese Megacity, *Environmental Science & Technology*, 53, 1822-1833, 10.1021/acs.est.8b05984, 2019.
- 840 Che, H., Zhang, X., Li, Y., Zhou, Z., Qu, J. J., and Hao, X.: Haze trends over the capital cities of 31 provinces in China, 1981–2005, *Theoretical and Applied Climatology*, 97, 235-242, 10.1007/s00704-008-0059-8, 2009.
- Chen, D., Liu, Z., Fast, J., and Ban, J.: Simulations of sulfate–nitrate–ammonium (SNA) aerosols during the extreme haze events over northern China in October 2014, *Atmos. Chem. Phys.*, 16, 10707-10724, 10.5194/acp-16-10707-2016, 2016.
- 845 Chen, Y., Shen, H., and Russell, A. G.: Current and Future Responses of Aerosol pH and Composition in the U.S. to Declining SO₂ Emissions and Increasing NH₃ Emissions, *Environmental Science & Technology*, 53, 9646-9655, 10.1021/acs.est.9b02005, 2019.
- Chen, Y., Cheng, Y., Ma, N., Wei, C., Ran, L., Wolke, R., Größ, J., Wang, Q., Pozzer, A., Denier van der Gon, H. A. C., Spindler, G., Lelieveld, J., Tegen, I., Su, H., and Wiedensohler, A.: Natural sea-salt emissions moderate the climate forcing of anthropogenic nitrate, *Atmos. Chem. Phys.*, 20, 771-786, 10.5194/acp-20-771-2020, 2020.
- 850 Chen, Y., Shen, H., Kaiser, J., Hu, Y., Capps, S. L., Zhao, S., Hakami, A., Shih, J. S., Pavur, G. K., Turner, M. D., Henze, D. K., Resler, J., Nenes, A., Napelenok, S. L., Bash, J. O., Fahey, K. M., Carmichael, G. R., Chai, T., Clarisse, L., Coheur, P. F., Van Damme, M., and Russell, A. G.: High-resolution hybrid inversion of IASI ammonia columns to constrain US ammonia emissions using the CMAQ adjoint model, *Atmos. Chem. Phys.*, 21, 2067-2082, 10.5194/acp-21-2067-2021, 2021.
- 855



- Cheng, Y., Zheng, G., Wei, C., Mu, Q., Zheng, B., Wang, Z., Gao, M., Zhang, Q., He, K., Carmichael, G., Pöschl, U., and Su, H.: Reactive nitrogen chemistry in aerosol water as a source of sulfate during haze events in China, *Science Advances*, 2, e1601530, doi:10.1126/sciadv.1601530, 2016.
- 860 Clarisse, L., Clerbaux, C., Dentener, F., Hurtmans, D., and Coheur, P.-F.: Global ammonia distribution derived from infrared satellite observations, *Nature Geoscience*, 2, 479–483, 10.1038/ngeo551, 2009.
- Colette, A., Granier, C., Hodnebrog, Ø., Jakobs, H., Maurizi, A., Nyiri, A., Bessagnet, B., D'Angiola, A., D'Isidoro, M., Gauss, M., Meleux, F., Memmesheimer, M., Mieville, A., Rouïl, L., Russo, F., Solberg, S., Stordal, F., and Tampieri, F.: Air quality trends in Europe over the past decade: a first multi-model assessment, *Atmos. Chem. Phys.*, 11, 11657–11678, 10.5194/acp-11-11657-2011, 2011.
- 865 Craig, R. L., Peterson, P. K., Nandy, L., Lei, Z., Hossain, M. A., Camarena, S., Dodson, R. A., Cook, R. D., Dutcher, C. S., and Ault, A. P.: Direct Determination of Aerosol pH: Size-Resolved Measurements of Submicrometer and Supermicrometer Aqueous Particles, *Analytical Chemistry*, 90, 11232–11239, 10.1021/acs.analchem.8b00586, 2018.
- 870 Crippa, M., Guizzardi, D., Muntean, M., Schaaf, E., Dentener, F., van Aardenne, J. A., Monni, S., Doering, U., Olivier, J. G. J., Pagliari, V., and Janssens-Maenhout, G.: Gridded emissions of air pollutants for the period 1970–2012 within EDGAR v4.3.2, *Earth Syst. Sci. Data*, 10, 1987–2013, 10.5194/essd-10-1987-2018, 2018.
- Dammers, E., McLinden, C. A., Griffin, D., Shephard, M. W., Van Der Graaf, S., Lutsch, E., Schaap, M., Gainairu-Matz, Y., Fioletov, V., Van Damme, M., Whitburn, S., Clarisse, L., Cady-Pereira, K., Clerbaux, C., Coheur, P. F., and Erismann, J. W.: NH₃ emissions from large point sources derived from CrIS and IASI satellite observations, *Atmos. Chem. Phys.*, 19, 12261–12293, 10.5194/acp-19-12261-2019, 2019.
- 875 Dammers, E., Shephard, M. W., Palm, M., Cady-Pereira, K., Capps, S., Lutsch, E., Strong, K., Hannigan, J. W., Ortega, I., Toon, G. C., Stremme, W., Grutter, M., Jones, N., Smale, D., Siemons, J., Hrpcek, K., Tremblay, D., Schaap, M., Notholt, J., and Erismann, J. W.: Validation of the CrIS fast physical NH₃ retrieval with ground-based FTIR, *Atmos. Meas. Tech.*, 10, 2645–2667, 10.5194/amt-10-2645-2017, 2017.
- 880 Delon, C., Galy-Lacaux, C., Adon, M., Liousse, C., Serça, D., Diop, B., and Akpo, A.: Nitrogen compounds emission and deposition in West African ecosystems: comparison between wet and dry savanna, *Biogeosciences*, 9, 385–402, 10.5194/bg-9-385-2012, 2012.
- Dentener, F. J. and Crutzen, P. J.: A three-dimensional model of the global ammonia cycle, *Journal of Atmospheric Chemistry*, 19, 331–369, 10.1007/BF00694492, 1994.
- 885 Ding, J., Zhao, P., Su, J., Dong, Q., Du, X., and Zhang, Y.: Aerosol pH and its driving factors in Beijing, *Atmos. Chem. Phys.*, 19, 7939–7954, 10.5194/acp-19-7939-2019, 2019.
- Dockery, D. W., Pope, C. A., Xu, X., Spengler, J. D., Ware, J. H., Fay, M. E., Ferris, B. G., and Speizer, F. E.: An Association between Air Pollution and Mortality in Six U.S. Cities, *New England Journal of Medicine*, 329, 1753–1759, 10.1056/nejm199312093292401, 1993.
- 890 Dockery, D. W., Cunningham, J., Damokosh, A. I., Neas, L. M., Spengler, J. D., Koutrakis, P., Ware, J. H., Raizenne, M., and Speizer, F. E.: Health effects of acid aerosols on North American children: respiratory symptoms, *Environmental Health Perspectives*, 104, 500–505, doi:10.1289/ehp.96104500, 1996.
- Erismann, J. W. and Schaap, M.: The need for ammonia abatement with respect to secondary PM reductions in Europe, *Environ Pollut*, 129, 159–163, 10.1016/j.envpol.2003.08.042, 2004.
- 895 Fang, T., Guo, H., Zeng, L., Verma, V., Nenes, A., and Weber, R. J.: Highly Acidic Ambient Particles, Soluble Metals, and Oxidative Potential: A Link between Sulfate and Aerosol Toxicity, *Environmental Science & Technology*, 51, 2611–2620, 10.1021/acs.est.6b06151, 2017.
- Fiddes, S. L., Woodhouse, M. T., Nicholls, Z., Lane, T. P., and Schofield, R.: Cloud, precipitation and radiation responses to large perturbations in global dimethyl sulfide, *Atmos. Chem. Phys.*, 18, 10177–10198, 10.5194/acp-18-10177-2018, 2018.
- 900 Fortems-Cheiney, A., Dufour, G., Foret, G., Siour, G., Van Damme, M., Coheur, P.-F., Clarisse, L., Clerbaux, C., and Beekmann, M.: Understanding the Simulated Ammonia Increasing Trend from 2008 to 2015 over Europe with CHIMERE and Comparison with IASI Observations, *Atmosphere*, 13, 1101, 2022.
- 905 Fountoukis, C. and Nenes, A.: ISORROPIA II: a computationally efficient thermodynamic equilibrium model for K^{+} – Ca^{2+} – Mg^{2+} – NH_4^{+} – Na^{+} – SO_4^{2-} – NO_3^{-} – Cl^{-} – H_2O aerosols, *Atmos. Chem. Phys.*, 7, 4639–4659, 10.5194/acp-7-4639-2007, 2007.
- 910 Fu, X., Wang, S., Xing, J., Zhang, X., Wang, T., and Hao, J.: Increasing Ammonia Concentrations Reduce the Effectiveness of Particle Pollution Control Achieved via SO₂ and NO_x Emissions Reduction in East China, *Environmental Science & Technology Letters*, 4, 221–227, 10.1021/acs.estlett.7b00143, 2017.



- Ge, Y., Vieno, M., Stevenson, D. S., Wind, P., and Heal, M. R.: A new assessment of global and regional budgets, fluxes, and lifetimes of atmospheric reactive N and S gases and aerosols, *Atmos. Chem. Phys.*, 22, 8343–8368, 10.5194/acp-22-8343-2022, 2022.
- 915 Gong, C., Tian, H., Liao, H., Pan, N., Pan, S., Ito, A., Jain, A. K., Kou-Giesbrecht, S., Joos, F., Sun, Q., Shi, H., Vuichard, N., Zhu, Q., Peng, C., Maggi, F., Tang, F. H. M., and Zaehele, S.: Global net climate effects of anthropogenic reactive nitrogen, *Nature*, 632, 557–563, 10.1038/s41586-024-07714-4, 2024.
- 920 Gu, B., Zhang, L., Van Dingenen, R., Vieno, M., Van Grinsven, H. J., Zhang, X., Zhang, S., Chen, Y., Wang, S., Ren, C., Rao, S., Holland, M., Winiwarter, W., Chen, D., Xu, J., and Sutton, M. A.: Abating ammonia is more cost-effective than nitrogen oxides for mitigating PM_{2.5} air pollution, *Science*, 374, 758–762, doi:10.1126/science.abf8623, 2021.
- Guo, H., Weber, R. J., and Nenes, A.: High levels of ammonia do not raise fine particle pH sufficiently to yield nitrogen oxide-dominated sulfate production, *Scientific Reports*, 7, 12109, 10.1038/s41598-017-11704-0, 2017a.
- 925 Guo, H., Otjes, R., Schlag, P., Kiendler-Scharr, A., Nenes, A., and Weber, R. J.: Effectiveness of ammonia reduction on control of fine particle nitrate, *Atmos. Chem. Phys.*, 18, 12241–12256, 10.5194/acp-18-12241-2018, 2018.
- Guo, H., Liu, J., Froyd, K. D., Roberts, J. M., Veres, P. R., Hayes, P. L., Jimenez, J. L., Nenes, A., and Weber, R. J.: Fine particle pH and gas–particle phase partitioning of inorganic species in Pasadena, California, during the 2010 CalNex campaign, *Atmos. Chem. Phys.*, 17, 5703–5719, 10.5194/acp-17-5703-2017, 2017b.
- 930 Guo, H., Sullivan, A. P., Campuzano-Jost, P., Schroder, J. C., Lopez-Hilfiker, F. D., Dibb, J. E., Jimenez, J. L., Thornton, J. A., Brown, S. S., Nenes, A., and Weber, R. J.: Fine particle pH and the partitioning of nitric acid during winter in the northeastern United States, *Journal of Geophysical Research: Atmospheres*, 121, 10,355–310,376, <https://doi.org/10.1002/2016JD025311>, 2016.
- 935 Guo, H., Xu, L., Bougiatioti, A., Cerully, K. M., Capps, S. L., Hite Jr, J. R., Carlton, A. G., Lee, S. H., Bergin, M. H., Ng, N. L., Nenes, A., and Weber, R. J.: Fine-particle water and pH in the southeastern United States, *Atmos. Chem. Phys.*, 15, 5211–5228, 10.5194/acp-15-5211-2015, 2015.
- Hand, J. L., Schichtel, B. A., Malm, W. C., and Pitchford, M. L.: Particulate sulfate ion concentration and SO₂ emission trends in the United States from the early 1990s through 2010, *Atmos. Chem. Phys.*, 12, 10353–10365, 10.5194/acp-12-10353-2012, 2012.
- 940 Hauglustaine, D. A., Balkanski, Y., and Schulz, M.: A global model simulation of present and future nitrate aerosols and their direct radiative forcing of climate, *Atmos. Chem. Phys.*, 14, 11031–11063, 10.5194/acp-14-11031-2014, 2014.
- Heald, C. L., Collett Jr, J. L., Lee, T., Benedict, K. B., Schwandner, F. M., Li, Y., Clarisse, L., Hurtmans, D. R., Van Damme, M., Clerbaux, C., Coheur, P. F., Philip, S., Martin, R. V., and Pye, H. O. T.: Atmospheric ammonia and particulate inorganic nitrogen over the United States, *Atmos. Chem. Phys.*, 12, 10295–10312, 10.5194/acp-12-10295-2012, 2012.
- 945 Hersbach, H., Bell, B., Berrisford, P., Hirahara, S., Horányi, A., Muñoz-Sabater, J., Nicolas, J., Peubey, C., Radu, R., Schepers, D., Simmons, A., Soci, C., Abdalla, S., Abellan, X., Balsamo, G., Bechtold, P., Biavati, G., Bidlot, J., Bonavita, M., De Chiara, G., Dahlgren, P., Dee, D., Diamantakis, M., Dragani, R., Flemming, J., Forbes, R., Fuentes, M., Geer, A., Haimberger, L., Healy, S., Hogan, R. J., Hólm, E., Janisková, M., Keeley, S., Laloyaux, P., Lopez, P., Lupu, C., Radnoti, G., de Rosnay, P., Rozum, I., Vamborg, F., Villaume, S., and Thépaut, J.-N.: The ERA5 global reanalysis, *Quarterly Journal of the Royal Meteorological Society*, 146, 1999–2049, <https://doi.org/10.1002/qj.3803>, 2020.
- 950 Hickman, J. E., Andela, N., Tsigaridis, K., Galy-Lacaux, C., Ossohou, M., Dammers, E., Van Damme, M., Clarisse, L., and Bauer, S. E.: Continental and Ecoregion-Specific Drivers of Atmospheric NO₂ and NH₃ Seasonality Over Africa Revealed by Satellite Observations, *Global Biogeochemical Cycles*, 35, e2020GB006916, <https://doi.org/10.1029/2020GB006916>, 2021.
- 955 Hoesly, R. M., Smith, S. J., Feng, L., Klimont, Z., Janssens-Maenhout, G., Pitkanen, T., Seibert, J. J., Vu, L., Andres, R. J., Bolt, R. M., Bond, T. C., Dawidowski, L., Kholod, N., Kurokawa, J. I., Li, M., Liu, L., Lu, Z., Moura, M. C. P., O'Rourke, P. R., and Zhang, Q.: Historical (1750–2014) anthropogenic emissions of reactive gases and aerosols from the Community Emissions Data System (CEDS), *Geosci. Model Dev.*, 11, 369–408, 10.5194/gmd-11-369-2018, 2018.
- 960 Huang, X., Zhang, J., Zhang, W., Tang, G., and Wang, Y.: Atmospheric ammonia and its effect on PM_{2.5} pollution in urban Chengdu, Sichuan Basin, China, *Environmental Pollution*, 291, 118195, <https://doi.org/10.1016/j.envpol.2021.118195>, 2021.
- 965 Intergovernmental Panel on Climate, C. (Ed.): *Climate Change 2022 - Mitigation of Climate Change: Working Group III Contribution to the Sixth Assessment Report of the Intergovernmental Panel on Climate Change*, Cambridge University Press, Cambridge, DOI: 10.1017/9781009157926, 2023.



- IPCC: Climate Change 2013: The Physical Science Basis. Contribution of Working Group I to the Fifth Assessment Report of the Intergovernmental Panel on Climate Change, Cambridge, United Kingdom and New York, NY, USA, 1535, 2013.
- Jackson, R. L., Gabric, A. J., Cropp, R., and Woodhouse, M. T.: Dimethylsulfide (DMS), marine biogenic aerosols and the ecophysiology of coral reefs, *Biogeosciences*, 17, 2181-2204, 10.5194/bg-17-2181-2020, 2020.
- Jo, Y.-J., Lee, H.-J., Jo, H.-Y., Woo, J.-H., Kim, Y., Lee, T., Heo, G., Park, S.-M., Jung, D., Park, J., and Kim, C.-H.: Changes in inorganic aerosol compositions over the Yellow Sea area from impact of Chinese emissions mitigation, *Atmospheric Research*, 240, 104948, <https://doi.org/10.1016/j.atmosres.2020.104948>, 2020.
- Jöckel, P., Sander, R., Kerkweg, A., Tost, H., and Lelieveld, J.: Technical Note: The Modular Earth Submodel System (MESSy) - a new approach towards Earth System Modeling, *Atmos. Chem. Phys.*, 5, 433-444, 10.5194/acp-5-433-2005, 2005.
- Jöckel, P., Kerkweg, A., Pozzer, A., Sander, R., Tost, H., Riede, H., Baumgaertner, A., Gromov, S., and Kern, B.: Development cycle 2 of the Modular Earth Submodel System (MESSy2), *Geosci. Model Dev.*, 3, 717-752, 10.5194/gmd-3-717-2010, 2010.
- Jöckel, P., Tost, H., Pozzer, A., Kunze, M., Kirner, O., Brenninkmeijer, C., Brinkop, S., Cai, D. S., Dyroff, C., and Eckstein, J.: Earth System Chemistry Integrated Modelling (ESCiMo) with the Modular Earth Submodel System (MESSy, version 2.51), *Geoscientific Model Development*, 9, 3(2016-03-31), 9, 1153-1200, 2016.
- Kaiser, J. W., Heil, A., Andreae, M. O., Benedetti, A., Chubarova, N., Jones, L., Morcrette, J. J., Razinger, M., Schultz, M. G., Suttie, M., and van der Werf, G. R.: Biomass burning emissions estimated with a global fire assimilation system based on observed fire radiative power, *Biogeosciences*, 9, 527-554, 10.5194/bg-9-527-2012, 2012.
- Kakavas, S., Patoulias, D., Zakoura, M., Nenes, A., and Pandis, S. N.: Size-resolved aerosol pH over Europe during summer, *Atmos. Chem. Phys.*, 21, 799-811, 10.5194/acp-21-799-2021, 2021.
- Karydis, V. A., Tsimpidi, A. P., Pozzer, A., and Lelieveld, J.: How alkaline compounds control atmospheric aerosol particle acidity, *Atmos. Chem. Phys.*, 21, 14983-15001, 10.5194/acp-21-14983-2021, 2021.
- Karydis, V. A., Tsimpidi, A. P., Lei, W., Molina, L. T., and Pandis, S. N.: Formation of semivolatile inorganic aerosols in the Mexico City Metropolitan Area during the MILAGRO campaign, *Atmos. Chem. Phys.*, 11, 13305-13323, 10.5194/acp-11-13305-2011, 2011.
- Karydis, V. A., Tsimpidi, A. P., Pozzer, A., Astitha, M., and Lelieveld, J.: Effects of mineral dust on global atmospheric nitrate concentrations, *Atmos. Chem. Phys.*, 16, 1491-1509, 10.5194/acp-16-1491-2016, 2016.
- Karydis, V. A., Tsimpidi, A. P., Bacer, S., Pozzer, A., Nenes, A., and Lelieveld, J.: Global impact of mineral dust on cloud droplet number concentration, *Atmos. Chem. Phys.*, 17, 5601-5621, 10.5194/acp-17-5601-2017, 2017.
- Karydis, V. A., Tsimpidi, A. P., Fountoukis, C., Nenes, A., Zavala, M., Lei, W., Molina, L. T., and Pandis, S. N.: Simulating the fine and coarse inorganic particulate matter concentrations in a polluted megacity, *Atmospheric Environment*, 44, 608-620, <https://doi.org/10.1016/j.atmosenv.2009.11.023>, 2010.
- Kerkweg, A., Buchholz, J., Ganzeveld, L., Pozzer, A., Tost, H., and Jöckel, P.: Technical Note: An implementation of the dry removal processes DRY DEPOSITION and SEDIMENTATION in the Modular Earth Submodel System (MESSy), *Atmos. Chem. Phys.*, 6, 4617-4632, 10.5194/acp-6-4617-2006, 2006.
- Khan, M. A. H., Lowe, D., Derwent, R. G., Foulds, A., Chhantyal-Pun, R., McFiggans, G., Orr-Ewing, A. J., Percival, C. J., and Shallcross, D. E.: Global and regional model simulations of atmospheric ammonia, *Atmospheric Research*, 234, 104702, <https://doi.org/10.1016/j.atmosres.2019.104702>, 2020.
- Klingmüller, K., Metzger, S., Abdelkader, M., Karydis, V. A., Stenchikov, G. L., Pozzer, A., and Lelieveld, J.: Revised mineral dust emissions in the atmospheric chemistry-climate model EMAC (MESSy 2.52 DU_Astitha1 KKDU2017 patch), *Geosci. Model Dev.*, 11, 989-1008, 10.5194/gmd-11-989-2018, 2018.
- Koçak, M., Mihalopoulos, N., and Kubilay, N.: Chemical composition of the fine and coarse fraction of aerosols in the northeastern Mediterranean, *Atmospheric Environment*, 41, 7351-7368, <https://doi.org/10.1016/j.atmosenv.2007.05.011>, 2007.
- Kong, L., Tang, X., Zhu, J., Wang, Z., Pan, Y., Wu, H., Wu, L., Wu, Q., He, Y., Tian, S., Xie, Y., Liu, Z., Sui, W., Han, L., and Carmichael, G.: Improved Inversion of Monthly Ammonia Emissions in China Based on the Chinese Ammonia Monitoring Network and Ensemble Kalman Filter, *Environmental Science & Technology*, 53, 12529-12538, 10.1021/acs.est.9b02701, 2019.
- Lei, L., Zhou, W., Chen, C., He, Y., Li, Z., Sun, J., Tang, X., Fu, P., Wang, Z., and Sun, Y.: Long-term characterization of aerosol chemistry in cold season from 2013 to 2020 in Beijing, China, *Environmental Pollution*, 268, 115952, <https://doi.org/10.1016/j.envpol.2020.115952>, 2021.
- Li, C., Martin, R. V., van Donkelaar, A., Boys, B. L., Hammer, M. S., Xu, J.-W., Marais, E. A., Reff, A., Strum, M., Ridley, D. A., Crippa, M., Brauer, M., and Zhang, Q.: Trends in Chemical Composition of Global and Regional Population-Weighted Fine Particulate Matter Estimated for 25 Years, *Environmental Science & Technology*, 51,



- 1025 11185-11195, 10.1021/acs.est.7b02530, 2017.
- Li, K., Chen, L., White, S. J., Yu, H., Wu, X., Gao, X., Azzi, M., and Cen, K.: Smog chamber study of the role of NH₃ in new particle formation from photo-oxidation of aromatic hydrocarbons, *Science of The Total Environment*, 619-620, 927-937, <https://doi.org/10.1016/j.scitotenv.2017.11.180>, 2018.
- 1030 Liu, J., Ding, P., Zong, Z., Li, J., Tian, C., Chen, W., Chang, M., Salazar, G., Shen, C., Cheng, Z., Chen, Y., Wang, X., Szidat, S., and Zhang, G.: Evidence of Rural and Suburban Sources of Urban Haze Formation in China: A Case Study From the Pearl River Delta Region, *Journal of Geophysical Research: Atmospheres*, 123, 4712-4726, <https://doi.org/10.1029/2017JD027952>, 2018a.
- Liu, L., Xu, W., Lu, X., Zhong, B., Guo, Y., Lu, X., Zhao, Y., He, W., Wang, S., Zhang, X., Liu, X., and Vitousek, P.: Exploring global changes in agricultural ammonia emissions and their contribution to nitrogen deposition since 1980, *Proceedings of the National Academy of Sciences*, 119, e2121998119, doi:10.1073/pnas.2121998119, 2022.
- 1035 Liu, M., Song, Y., Zhou, T., Xu, Z., Yan, C., Zheng, M., Wu, Z., Hu, M., Wu, Y., and Zhu, T.: Fine particle pH during severe haze episodes in northern China, *Geophysical Research Letters*, 44, 5213-5221, <https://doi.org/10.1002/2017GL073210>, 2017.
- Liu, M., Huang, X., Song, Y., Xu, T., Wang, S., Wu, Z., Hu, M., Zhang, L., Zhang, Q., Pan, Y., Liu, X., and Zhu, T.: Rapid SO₂ emission reductions significantly increase tropospheric ammonia concentrations over the North China Plain, *Atmos. Chem. Phys.*, 18, 17933-17943, 10.5194/acp-18-17933-2018, 2018b.
- Lohmann, U. and Ferrachat, S.: Impact of parametric uncertainties on the present-day climate and on the anthropogenic aerosol effect, *Atmos. Chem. Phys.*, 10, 11373-11383, 10.5194/acp-10-11373-2010, 2010.
- Luo, Z., Zhang, Y., Chen, W., Van Damme, M., Coheur, P. F., and Clarisse, L.: Estimating global ammonia (NH₃) emissions based on IASI observations from 2008 to 2018, *Atmos. Chem. Phys.*, 22, 10375-10388, 10.5194/acp-22-10375-2022, 2022.
- 1045 McDuffie, E. E., Smith, S. J., O'Rourke, P., Tibrewal, K., Venkataraman, C., Marais, E. A., Zheng, B., Crippa, M., Brauer, M., and Martin, R. V.: A global anthropogenic emission inventory of atmospheric pollutants from sector- and fuel-specific sources (1970–2017): an application of the Community Emissions Data System (CEDS), *Earth Syst. Sci. Data*, 12, 3413-3442, 10.5194/essd-12-3413-2020, 2020.
- 1050 Milousis, A., Tsimpidi, A. P., Tost, H., Pandis, S. N., Nenes, A., Kiendler-Scharr, A., and Karydis, V. A.: Implementation of the ISORROPIA-lite aerosol thermodynamics model into the EMAC chemistry climate model (based on MESSy v2.55): implications for aerosol composition and acidity, *Geosci. Model Dev.*, 17, 1111-1131, 10.5194/gmd-17-1111-2024, 2024.
- 1055 Morán, M., Ferreira, J., Martins, H., Monteiro, A., Borrego, C., and González, J. A.: Ammonia agriculture emissions: From EMEP to a high resolution inventory, *Atmospheric Pollution Research*, 7, 786-798, <https://doi.org/10.1016/j.apr.2016.04.001>, 2016.
- Nenes, A., Pandis, S. N., and Pilinis, C.: ISORROPIA: A New Thermodynamic Equilibrium Model for Multiphase Multicomponent Inorganic Aerosols, *Aquatic Geochemistry*, 4, 123-152, 10.1023/A:1009604003981, 1998.
- 1060 Nenes, A., Pandis, S. N., Weber, R. J., and Russell, A.: Aerosol pH and liquid water content determine when particulate matter is sensitive to ammonia and nitrate availability, *Atmos. Chem. Phys.*, 20, 3249-3258, 10.5194/acp-20-3249-2020, 2020.
- Olivier, J. G. J., Bouwman, A. F., Van der Hoek, K. W., and Berdowski, J. J. M.: Global air emission inventories for anthropogenic sources of NO_x, NH₃ and N₂O in 1990, *Environmental Pollution*, 102, 135-148, [https://doi.org/10.1016/S0269-7491\(98\)80026-2](https://doi.org/10.1016/S0269-7491(98)80026-2), 1998.
- 1065 Osipov, S., Chowdhury, S., Crowley, J. N., Tadic, I., Drewnick, F., Borrmann, S., Eger, P., Fachinger, F., Fischer, H., Predybaylo, E., Fnais, M., Harder, H., Pikridas, M., Vouterakos, P., Pozzer, A., Sciare, J., Ukhov, A., Stenchikov, G. L., Williams, J., and Lelieveld, J.: Severe atmospheric pollution in the Middle East is attributable to anthropogenic sources, *Communications Earth & Environment*, 3, 203, 10.1038/s43247-022-00514-6, 2022.
- 1070 Pan, Y., Tian, S., Liu, D., Fang, Y., Zhu, X., Zhang, Q., Zheng, B., Michalski, G., and Wang, Y.: Fossil Fuel Combustion-Related Emissions Dominate Atmospheric Ammonia Sources during Severe Haze Episodes: Evidence from (15)N-Stable Isotope in Size-Resolved Aerosol Ammonium, *Environ Sci Technol*, 50, 8049-8056, 10.1021/acs.est.6b00634, 2016.
- Pozzer, A., Reifenberg, S. F., Kumar, V., Franco, B., Kohl, M., Taraborrelli, D., Gromov, S., Ehrhart, S., Jöckel, P., Sander, R., Fall, V., Rosanka, S., Karydis, V., Akritidis, D., Emmenrichs, T., Crippa, M., Guizzardi, D., Kaiser, J. W., Clarisse, L., Kiendler-Scharr, A., Tost, H., and Tsimpidi, A.: Simulation of organics in the atmosphere: evaluation of EMACv2.54 with the Mainz Organic Mechanism (MOM) coupled to the ORACLE (v1.0) submodel, *Geosci. Model Dev.*, 15, 2673-2710, 10.5194/gmd-15-2673-2022, 2022.
- 1075 Pozzer, A., Tsimpidi, A. P., Karydis, V. A., de Meij, A., and Lelieveld, J.: Impact of agricultural emission reductions on fine-particulate matter and public health, *Atmos. Chem. Phys.*, 17, 12813-12826, 10.5194/acp-17-12813-2017,
- 1080



- 2017.
- Pringle, K. J., Tost, H., Message, S., Steil, B., Giannadaki, D., Nenes, A., Fountoukis, C., Stier, P., Vignati, E., and Lelieveld, J.: Description and evaluation of GMX: a new aerosol submodel for global simulations (v1), *Geosci. Model Dev.*, 3, 391-412, 10.5194/gmd-3-391-2010, 2010.
- 1085 Prospero, J. M., Savoie, D. L., Nees, R. T., Duce, R. A., and Merrill, J.: Particulate sulfate and nitrate in the boundary layer over the North Pacific Ocean, *Journal of Geophysical Research: Atmospheres*, 90, 10586-10596, <https://doi.org/10.1029/JD090iD06p10586>, 1985.
- Pye, H. O. T., Nenes, A., Alexander, B., Ault, A. P., Barth, M. C., Clegg, S. L., Collett Jr, J. L., Fahey, K. M., Hennigan, C. J., Herrmann, H., Kanakidou, M., Kelly, J. T., Ku, I. T., McNeill, V. F., Riemer, N., Schaefer, T., Shi, G., Tilgner, A., Walker, J. T., Wang, T., Weber, R., Xing, J., Zaveri, R. A., and Zuend, A.: The acidity of atmospheric particles and clouds, *Atmos. Chem. Phys.*, 20, 4809-4888, 10.5194/acp-20-4809-2020, 2020.
- 1090 Roeckner, E., Brokopf, R., Esch, M., Giorgetta, M., Hagemann, S., Kornbluh, L., Manzini, E., Schlese, U., and Schulzweida, U.: Sensitivity of simulated climate to horizontal and vertical resolution in the ECHAM5 atmosphere model, *Journal of Climate*, 19, 3771-3791, 10.1175/jcli3824.1, 2006.
- 1095 Russell, A. R., Valin, L. C., and Cohen, R. C.: Trends in OMI NO₂ observations over the United States: effects of emission control technology and the economic recession, *Atmos. Chem. Phys.*, 12, 12197-12209, 10.5194/acp-12-12197-2012, 2012.
- Russell, L. M., Moore, R. H., Burrows, S. M., and Quinn, P. K.: Ocean flux of salt, sulfate, and organic components to atmospheric aerosol, *Earth-Science Reviews*, 239, 104364, <https://doi.org/10.1016/j.earscirev.2023.104364>, 2023.
- 1100 Sahoo, P., Sahu, S. K., Mangaraj, P., Mishra, A., Beig, G., and Gunthe, S. S.: Reporting of gridded ammonia emission and assessment of hotspots across India: A comprehensive study of 24 anthropogenic sources, *Journal of Hazardous Materials*, 479, 135557, <https://doi.org/10.1016/j.jhazmat.2024.135557>, 2024.
- 1105 Sander, R., Baumgaertner, A., Cabrera-Perez, D., Frank, F., Gromov, S., Grooß, J. U., Harder, H., Huijnen, V., Jöckel, P., Karydis, V. A., Niemeyer, K. E., Pozzer, A., Riede, H., Schultz, M. G., Taraborrelli, D., and Tauer, S.: The community atmospheric chemistry box model CAABA/MECCA-4.0, *Geosci. Model Dev.*, 12, 1365-1385, 10.5194/gmd-12-1365-2019, 2019.
- Schlesinger, W. H. and Hartley, A. E.: A global budget for atmospheric NH₃, *Biogeochemistry*, 15, 191-211, 10.1007/BF00002936, 1992.
- 1110 Seinfeld, J. H. and Pandis, S. N.: *Atmospheric chemistry and physics : from air pollution to climate change*, Third edition, John Wiley & Sons, Inc. Hoboken, New Jersey, Hoboken, New Jersey 2016.
- Shah, V., Jaeglé, L., Thornton, J. A., Lopez-Hilfiker, F. D., Lee, B. H., Schroder, J. C., Campuzano-Jost, P., Jimenez, J. L., Guo, H., Sullivan, A. P., Weber, R. J., Green, J. R., Fiddler, M. N., Bililign, S., Campos, T. L., Stell, M., Weinheimer, A. J., Montzka, D. D., and Brown, S. S.: Chemical feedbacks weaken the wintertime response of particulate sulfate and nitrate to emissions reductions over the eastern United States, *Proceedings of the National Academy of Sciences*, 115, 8110-8115, doi:10.1073/pnas.1803295115, 2018.
- 1115 Shi, G., Xu, J., Peng, X., Xiao, Z., Chen, K., Tian, Y., Guan, X., Feng, Y., Yu, H., Nenes, A., and Russell, A. G.: pH of Aerosols in a Polluted Atmosphere: Source Contributions to Highly Acidic Aerosol, *Environmental Science & Technology*, 51, 4289-4296, 10.1021/acs.est.6b05736, 2017.
- 1120 Shi, G., Xu, J., Shi, X., Liu, B., Bi, X., Xiao, Z., Chen, K., Wen, J., Dong, S., Tian, Y., Feng, Y., Yu, H., Song, S., Zhao, Q., Gao, J., and Russell, A. G.: Aerosol pH Dynamics During Haze Periods in an Urban Environment in China: Use of Detailed, Hourly, Speciated Observations to Study the Role of Ammonia Availability and Secondary Aerosol Formation and Urban Environment, *Journal of Geophysical Research: Atmospheres*, 124, 9730-9742, <https://doi.org/10.1029/2018JD029976>, 2019.
- 1125 Skjøth, C. A. and Geels, C.: The effect of climate and climate change on ammonia emissions in Europe, *Atmos. Chem. Phys.*, 13, 117-128, 10.5194/acp-13-117-2013, 2013.
- Søgaard, H. T., Sommer, S. G., Hutchings, N. J., Huijsmans, J. F. M., Bussink, D. W., and Nicholson, F.: Ammonia volatilization from field-applied animal slurry—the ALFAM model, *Atmospheric Environment*, 36, 3309-3319, [https://doi.org/10.1016/S1352-2310\(02\)00300-X](https://doi.org/10.1016/S1352-2310(02)00300-X), 2002.
- 1130 Song, S., Nenes, A., Gao, M., Zhang, Y., Liu, P., Shao, J., Ye, D., Xu, W., Lei, L., Sun, Y., Liu, B., Wang, S., and McElroy, M. B.: Thermodynamic Modeling Suggests Declines in Water Uptake and Acidity of Inorganic Aerosols in Beijing Winter Haze Events during 2014/2015–2018/2019, *Environmental Science & Technology Letters*, 6, 752-760, 10.1021/acs.estlett.9b00621, 2019.
- 1135 Spengler, J. D., Koutrakis, P., Dockery, D. W., Raizenne, M., and Speizer, F. E.: Health effects of acid aerosols on North American children: air pollution exposures, *Environmental Health Perspectives*, 104, 492-499, doi:10.1289/ehp.96104492, 1996.



- Thurston, G. D., Ito, K., Hayes, C. G., Bates, D. V., and Lippmann, M.: Respiratory Hospital Admissions and
 Summertime Haze Air Pollution in Toronto, Ontario: Consideration of the Role of Acid Aerosols, *Environmental
 Research*, 65, 271-290, <https://doi.org/10.1006/enrs.1994.1037>, 1994.
- 1140 Tilgner, A., Schaefer, T., Alexander, B., Barth, M., Collett Jr, J. L., Fahey, K. M., Nenes, A., Pye, H. O. T., Herrmann,
 H., and McNeill, V. F.: Acidity and the multiphase chemistry of atmospheric aqueous particles and clouds, *Atmos.
 Chem. Phys.*, 21, 13483-13536, 10.5194/acp-21-13483-2021, 2021.
- Tost, H., Jöckel, P., Kerkweg, A., Sander, R., and Lelieveld, J.: Technical note: A new comprehensive SCAVenging
 submodel for global atmospheric chemistry modelling, *Atmos. Chem. Phys.*, 6, 565-574, 10.5194/acp-6-565-2006,
 1145 2006.
- Tsimpidi, A. P., Karydis, V. A., and Pandis, S. N.: Response of Inorganic Fine Particulate Matter to Emission Changes
 of Sulfur Dioxide and Ammonia: The Eastern United States as a Case Study, *Journal of the Air & Waste
 Management Association*, 57, 1489-1498, 10.3155/1047-3289.57.12.1489, 2007.
- 1150 Tsimpidi, A. P., Karydis, V. A., Pandis, S. N., and Lelieveld, J.: Global combustion sources of organic aerosols: model
 comparison with 84 AMS factor-analysis data sets, *Atmos. Chem. Phys.*, 16, 8939-8962, 10.5194/acp-16-8939-
 2016, 2016.
- Tsimpidi, A. P., Karydis, V. A., Pozzer, A., Pandis, S. N., and Lelieveld, J.: ORACLE (v1.0): module to simulate the
 organic aerosol composition and evolution in the atmosphere, *Geosci. Model Dev.*, 7, 3153-3172, 10.5194/gmd-
 7-3153-2014, 2014.
- 1155 van Aardenne, J. A., Dentener, F. J., Olivier, J. G. J., Goldewijk, C. G. M. K., and Lelieveld, J.: A $1^\circ \times 1^\circ$ resolution
 data set of historical anthropogenic trace gas emissions for the period 1890–1990, *Global Biogeochemical Cycles*,
 15, 909-928, <https://doi.org/10.1029/2000GB001265>, 2001.
- Van Damme, M., Clarisse, L., Whitburn, S., Hadji-Lazaro, J., Hurtmans, D., Clerbaux, C., and Coheur, P.-F.: Industrial
 and agricultural ammonia point sources exposed, *Nature*, 564, 99-103, 10.1038/s41586-018-0747-1, 2018.
- 1160 Van Damme, M., Erisman, J. W., Clarisse, L., Dammers, E., Whitburn, S., Clerbaux, C., Dolman, A. J., and Coheur,
 P.-F.: Worldwide spatiotemporal atmospheric ammonia (NH₃) columns variability revealed by satellite,
Geophysical Research Letters, 42, 8660-8668, <https://doi.org/10.1002/2015GL065496>, 2015.
- Van Damme, M., Clarisse, L., Heald, C. L., Hurtmans, D., Ngadi, Y., Clerbaux, C., Dolman, A. J., Erisman, J. W., and
 Coheur, P. F.: Global distributions, time series and error characterization of atmospheric ammonia
 (NH₃) from IASI satellite observations, *Atmos. Chem. Phys.*, 14, 2905-2922, 10.5194/acp-14-2905-
 2014, 2014.
- 1165 Vignati, E., Wilson, J., and Stier, P.: M7: An efficient size-resolved aerosol microphysics module for large-scale
 aerosol transport models, *Journal of Geophysical Research*, 109, 10.1029/2003JD004485, 2004.
- Walker, J. M., Philip, S., Martin, R. V., and Seinfeld, J. H.: Simulation of nitrate, sulfate, and ammonium aerosols over
 the United States, *Atmos. Chem. Phys.*, 12, 11213-11227, 10.5194/acp-12-11213-2012, 2012.
- 1170 Wang, G., Zhang, R., Gomez, M. E., Yang, L., Levy Zamora, M., Hu, M., Lin, Y., Peng, J., Guo, S., Meng, J., Li, J.,
 Cheng, C., Hu, T., Ren, Y., Wang, Y., Gao, J., Cao, J., An, Z., Zhou, W., Li, G., Wang, J., Tian, P., Marrero-Ortiz,
 W., Secrest, J., Du, Z., Zheng, J., Shang, D., Zeng, L., Shao, M., Wang, W., Huang, Y., Wang, Y., Zhu, Y., Li, Y.,
 Hu, J., Pan, B., Cai, L., Cheng, Y., Ji, Y., Zhang, F., Rosenfeld, D., Liss, P. S., Duce, R. A., Kolb, C. E., and Molina,
 M. J.: Persistent sulfate formation from London Fog to Chinese haze, *Proceedings of the National Academy of
 Sciences*, 113, 13630-13635, doi:10.1073/pnas.1616540113, 2016.
- 1175 Wang, M., Kong, W., Marten, R., He, X.-C., Chen, D., Pfeifer, J., Heitto, A., Kontkanen, J., Dada, L., Kürten, A., Yli-
 Juuti, T., Manninen, H. E., Amanatidis, S., Amorim, A., Baalbaki, R., Baccarini, A., Bell, D. M., Bertozzi, B.,
 Bräkling, S., Brilke, S., Murillo, L. C., Chiu, R., Chu, B., De Menezes, L.-P., Duplissy, J., Finkenzeller, H.,
 Carracedo, L. G., Granzin, M., Guida, R., Hansel, A., Hofbauer, V., Krechmer, J., Lehtipalo, K., Lamkaddam, H.,
 Lampimäki, M., Lee, C. P., Makhmutov, V., Marie, G., Mathot, S., Mauldin, R. L., Mentler, B., Müller, T., Onnela,
 A., Partoll, E., Petäjä, T., Philippov, M., Pospisilova, V., Ranjithkumar, A., Rissanen, M., Röhrup, B., Scholz, W.,
 Shen, J., Simon, M., Sipilä, M., Steiner, G., Stolzenburg, D., Tham, Y. J., Tomé, A., Wagner, A. C., Wang, D. S.,
 Wang, Y., Weber, S. K., Winkler, P. M., Wlasits, P. J., Wu, Y., Xiao, M., Ye, Q., Zauner-Wieczorek, M., Zhou, X.,
 Volkamer, R., Riipinen, I., Dommen, J., Curtius, J., Baltensperger, U., Kulmala, M., Worsnop, D. R., Kirkby, J.,
 Seinfeld, J. H., El-Haddad, I., Flagan, R. C., and Donahue, N. M.: Rapid growth of new atmospheric particles by
 nitric acid and ammonia condensation, *Nature*, 581, 184-189, 10.1038/s41586-020-2270-4, 2020.
- 1185 Wang, S., Xing, J., Jang, C., Zhu, Y., Fu, J. S., and Hao, J.: Impact Assessment of Ammonia Emissions on Inorganic
 Aerosols in East China Using Response Surface Modeling Technique, *Environmental Science & Technology*, 45,
 9293-9300, 10.1021/es2022347, 2011.
- 1190 Wang, X., Zhang, C., Gao, Y., Ji, X., Su, W., and Liu, C.: Satellite unravels recent changes in atmospheric nitrogen
 oxides emissions from global ocean shipping, *Journal of Cleaner Production*, 429, 139591,



- https://doi.org/10.1016/j.jclepro.2023.139591, 2023.
- 1195 Wang, X., Wang, W., Yang, L., Gao, X., Nie, W., Yu, Y., Xu, P., Zhou, Y., and Wang, Z.: The secondary formation of inorganic aerosols in the droplet mode through heterogeneous aqueous reactions under haze conditions, *Atmospheric Environment*, 63, 68-76, <https://doi.org/10.1016/j.atmosenv.2012.09.029>, 2012.
- Wang, Y., Zhang, Q. Q., He, K., Zhang, Q., and Chai, L.: Sulfate-nitrate-ammonium aerosols over China: response to 2000–2015 emission changes of sulfur dioxide, nitrogen oxides, and ammonia, *Atmos. Chem. Phys.*, 13, 2635–2652, 10.5194/acp-13-2635-2013, 2013.
- 1200 Warner, J. X., Dickerson, R. R., Wei, Z., Strow, L. L., Wang, Y., and Liang, Q.: Increased atmospheric ammonia over the world's major agricultural areas detected from space, *Geophysical Research Letters*, 44, 2875-2884, <https://doi.org/10.1002/2016GL072305>, 2017.
- Weber, R. J., Guo, H., Russell, A. G., and Nenes, A.: High aerosol acidity despite declining atmospheric sulfate concentrations over the past 15 years, *Nature Geoscience*, 9, 282-285, 10.1038/ngeo2665, 2016.
- 1205 West, J. J., Ansari, A. S., and Pandis, S. N.: Marginal PM_{2.5}: Nonlinear Aerosol Mass Response to Sulfate Reductions in the Eastern United States, *Journal of the Air & Waste Management Association*, 49, 1415-1424, 10.1080/10473289.1999.10463973, 1999.
- Xie, X., Hu, J., Qin, M., Guo, S., Hu, M., Wang, H., Lou, S., Li, J., Sun, J., Li, X., Sheng, L., Zhu, J., Chen, G., Yin, J., Fu, W., Huang, C., and Zhang, Y.: Modeling particulate nitrate in China: Current findings and future directions, *Environment International*, 166, 107369, <https://doi.org/10.1016/j.envint.2022.107369>, 2022.
- 1210 Xu, J., Chen, J., Zhao, N., Wang, G., Yu, G., Li, H., Huo, J., Lin, Y., Fu, Q., Guo, H., Deng, C., Lee, S. H., Chen, J., and Huang, K.: Importance of gas-particle partitioning of ammonia in haze formation in the rural agricultural environment, *Atmos. Chem. Phys.*, 20, 7259-7269, 10.5194/acp-20-7259-2020, 2020.
- Xu, P., Li, G., Zheng, Y., Fung, J. C. H., Chen, A., Zeng, Z., Shen, H., Hu, M., Mao, J., Zheng, Y., Cui, X., Guo, Z., Chen, Y., Feng, L., He, S., Zhang, X., Lau, A. K. H., Tao, S., and Houlton, B. Z.: Fertilizer management for global ammonia emission reduction, *Nature*, 626, 792-798, 10.1038/s41586-024-07020-z, 2024.
- 1215 Xu, P., Liao, Y. J., Lin, Y. H., Zhao, C. X., Yan, C. H., Cao, M. N., Wang, G. S., and Luan, S. J.: High-resolution inventory of ammonia emissions from agricultural fertilizer in China from 1978 to 2008, *Atmos. Chem. Phys.*, 16, 1207-1218, 10.5194/acp-16-1207-2016, 2016.
- 1220 Xu, R., Tian, H., Pan, S., Prior, S. A., Feng, Y., Batchelor, W. D., Chen, J., and Yang, J.: Global ammonia emissions from synthetic nitrogen fertilizer applications in agricultural systems: Empirical and process-based estimates and uncertainty, *Global Change Biology*, 25, 314-326, <https://doi.org/10.1111/gcb.14499>, 2019.
- Yao, W., Zhang, C., Hao, H., Wang, X., and Li, X.: A support vector machine approach to estimate global solar radiation with the influence of fog and haze, *Renewable Energy*, 128, 155-162, <https://doi.org/10.1016/j.renene.2018.05.069>, 2018.
- 1225 Yu, F., Nair, A. A., and Luo, G.: Long-Term Trend of Gaseous Ammonia Over the United States: Modeling and Comparison With Observations, *Journal of Geophysical Research: Atmospheres*, 123, 8315-8325, <https://doi.org/10.1029/2018JD028412>, 2018.
- Zhang, B., Shen, H., Liu, P., Guo, H., Hu, Y., Chen, Y., Xie, S., Xi, Z., Skipper, T. N., and Russell, A. G.: Significant contrasts in aerosol acidity between China and the United States, *Atmos. Chem. Phys.*, 21, 8341-8356, 10.5194/acp-21-8341-2021, 2021a.
- 1230 Zhang, L., Chen, Y., Zhao, Y., Henze, D. K., Zhu, L., Song, Y., Paulot, F., Liu, X., Pan, Y., Lin, Y., and Huang, B.: Agricultural ammonia emissions in China: reconciling bottom-up and top-down estimates, *Atmos. Chem. Phys.*, 18, 339-355, 10.5194/acp-18-339-2018, 2018.
- 1235 Zhang, L., Gong, S., Zhao, T., Zhou, C., Wang, Y., Li, J., Ji, D., He, J., Liu, H., Gui, K., Guo, X., Gao, J., Shan, Y., Wang, H., Wang, Y., Che, H., and Zhang, X.: Development of WRF/CUACE v1.0 model and its preliminary application in simulating air quality in China, *Geosci. Model Dev.*, 14, 703-718, 10.5194/gmd-14-703-2021, 2021b.
- Zhang, Q. and Geng, G.: Impact of clean air action on PM_{2.5} pollution in China, *Science China Earth Sciences*, 62, 1845-1846, 10.1007/s11430-019-9531-4, 2019.
- 1240 Zhao, P., Zhang, X., Xu, X., and Zhao, X.: Long-term visibility trends and characteristics in the region of Beijing, Tianjin, and Hebei, China, *Atmospheric Research*, 101, 711-718, <https://doi.org/10.1016/j.atmosres.2011.04.019>, 2011.
- Zheng, B., Zhang, Q., Zhang, Y., He, K. B., Wang, K., Zheng, G. J., Duan, F. K., Ma, Y. L., and Kimoto, T.: Heterogeneous chemistry: a mechanism missing in current models to explain secondary inorganic aerosol formation during the January 2013 haze episode in North China, *Atmos. Chem. Phys.*, 15, 2031-2049, 10.5194/acp-15-2031-2015, 2015.
- 1245 Zheng, B., Tong, D., Li, M., Liu, F., Hong, C., Geng, G., Li, H., Li, X., Peng, L., Qi, J., Yan, L., Zhang, Y., Zhao, H.,



- 1250 Zheng, Y., He, K., and Zhang, Q.: Trends in China's anthropogenic emissions since 2010 as the consequence of clean air actions, *Atmos. Chem. Phys.*, 18, 14095-14111, 10.5194/acp-18-14095-2018, 2018.
- Zheng, G., Su, H., and Cheng, Y.: Revisiting the Key Driving Processes of the Decadal Trend of Aerosol Acidity in the U.S, *ACS Environmental Au*, 2, 346-353, 10.1021/acsenvironau.1c00055, 2022.
- Zheng, G., Su, H., Andreae, M. O., Pöschl, U., and Cheng, Y.: Multiphase Buffering by Ammonia Sustains Sulfate Production in Atmospheric Aerosols, *AGU Advances*, 5, e2024AV001238, 1255 <https://doi.org/10.1029/2024AV001238>, 2024.
- Zheng, G., Su, H., Wang, S., Andreae, M. O., Pöschl, U., and Cheng, Y.: Multiphase buffer theory explains contrasts in atmospheric aerosol acidity, *Science*, 369, 1374-1377, doi:10.1126/science.aba3719, 2020.
- Zhou, M., Deng, Z., Robert, C., Zhang, X., Zhang, L., Wang, Y., Qi, C., Wang, P., and Mazière, M. D.: The First Global Map of Atmospheric Ammonia (NH₃) as Observed by the HIRAS/FY-3D Satellite, *Advances in Atmospheric Sciences*, 41, 379-390, 10.1007/s00376-023-3059-9, 2024.
- 1260 Zhou, M., Zheng, G., Wang, H., Qiao, L., Zhu, S., Huang, D., An, J., Lou, S., Tao, S., Wang, Q., Yan, R., Ma, Y., Chen, C., Cheng, Y., Su, H., and Huang, C.: Long-term trends and drivers of aerosol pH in eastern China, *Atmos. Chem. Phys.*, 22, 13833-13844, 10.5194/acp-22-13833-2022, 2022.
- 1265 Zhou, W., Gao, M., He, Y., Wang, Q., Xie, C., Xu, W., Zhao, J., Du, W., Qiu, Y., Lei, L., Fu, P., Wang, Z., Worsnop, D. R., Zhang, Q., and Sun, Y.: Response of aerosol chemistry to clean air action in Beijing, China: Insights from two-year ACSM measurements and model simulations, *Environmental Pollution*, 255, 113345, <https://doi.org/10.1016/j.envpol.2019.113345>, 2019.